

Optimization of Ion-Cyclotron Range of
Frequency Wave Heating in
the Minimum-B Configuration on GAMMA 10

Takuro YOKOYAMA

Doctoral Program in Applied Physics

Submitted to the Graduate School of
Pure and Applied Sciences
in Partial Fulfillment of the Requirements
for the Degree of Doctor of Philosophy in
Engineering

at the
University of Tsukuba

Abstract

This thesis describes the optimization of plasma heating by waves in the ion cyclotron range of frequency (ICRF) in the minimum-B anchor configuration on GAMMA 10.

On the nuclear fusion reactors in the magnetic confinement systems, it needs to research about heating plasmas, controlling instabilities, plasma-wall interactions, and so on. GAMMA 10, which is the world largest tandem mirror device, has high temperature ions produced by ICRF waves, and the open magnetic field configuration at the both ends. The divertor simulation experiments progresses with high temperature and open magnetic configuration. In this experiments, it is required to produce and control high temperature and high density plasmas. It is indicated in the experiments that the increase of particle flux at the end of GAMMA 10 is achieved by the high density plasmas. On GAMMA 10, the high- β plasmas in the anchor cell are essential to keep high pressure plasmas stably, because the high- β plasmas in the anchor cell are kept the magneto hydro dynamic stability. In order to produce high- β plasmas more effectively, the enhancement of anchor heating is introduced.

In order to enhance ion-heating in the anchor cell, the enhancement antenna loading of the anchor ICRF antenna is introduced. The anchor ICRF antenna, which are designed to be along the shape of the plasma cross section for enhancement of antenna loading, have been newly installed in the anchor cell. It is observed that the antenna loading of the anchor antenna increases and the enhancement of the anchor heating is more efficient.

In order to achieve more efficient anchor heating, the phase-control experiments are introduced on GAMMA 10. The phase-control experiments are achieved by wave interference using two ICRF antennas installed in the central cell and the anchor cell. In the phase-control experiments, the enhancement of the ion heating in the anchor cell and the increase of the density in the anchor and central cells are clearly observed depending on the phase difference between two antennas. In order to analyze wave propagation and the absorbed RF power in the phase-control experiments, three dimensional full wave code (TASK/WF) is introduced. In TASK/WF, the absorbed powers on the resonance layer in the phase control experiments are calculated. It is clearly indicated that the absorbed power depends on the phase difference between two antennas. It is clearly obtained that the phase difference at the maximum

absorbed power is the optimum condition in the experiments.

According to the results of the anchor heating experiments and the numerical simulation, the enhancement of the antenna loading and the optimization of the phase difference between two antennas will be essential for the increase of the plasma performance such as the density and the particle flux for experiments.

Contents

| | | |
|----------|---|-----------|
| 1 | Introduction | 1 |
| 2 | Experimental Setup | 4 |
| 2.1 | Principle of confinement in the magnetic mirror | 4 |
| 2.2 | GAMMA10 tandem mirror device | 6 |
| 2.2.1 | Magnetic Mirror Configuration on GAMMA 10 | 6 |
| 2.2.2 | Configuration of GAMMA 10 | 6 |
| 2.2.3 | Gas Fueling System and Plasma Gun | 8 |
| 2.2.4 | Electron Cyclotron Resonance Heating and Neutral Beam Injection systems | 9 |
| 2.3 | Ion Cyclotron Range of Frequency (ICRF) Heating | 10 |
| 2.3.1 | ICRF Systems | 10 |
| 2.3.2 | ICRF Antennas | 10 |
| 2.3.3 | Anchor Heating for Magneto-Hydro Dynamic (MHD) stabilization | 15 |
| 2.4 | Diagnostics | 17 |
| 2.4.1 | Measurements Instruments for ICRF Heating | 17 |
| 2.4.1.1 | Secondary Electron Detector | 17 |
| 2.4.1.2 | Current pick-up coils | 19 |
| 2.4.1.3 | Measurement of ICRF power | 19 |
| 2.4.2 | Fundamental Measurement Instruments | 21 |
| 2.4.2.1 | Diamagnetic loop | 21 |
| 2.4.2.2 | Microwave Interferometer | 23 |
| 2.4.2.2 | CX-NPA | 25 |
| 2.4.2.4 | Electro Static Probe and Segment Limiter | 25 |
| 3 | Three Dimensional Full Wave Code | 27 |
| 3.1 | Three dimensional full wave simulation | 27 |
| 3.1.1 | Basic Equation | 27 |

| | | |
|----------|--|-----------|
| 3.2.1 | Boundary condition | 30 |
| 3.3 | Introduction of Multi-Processing Code | 30 |
| 3.4 | Setup for GAMMA 10 | 31 |
| 3.4.1 | Calculation Elements | 31 |
| 3.4.2 | Parameters for Wave Analysis | 32 |
| 4 | Experimental Observation of Antenna Modification | 37 |
| 4.1 | Antenna Loading of Anchor ICRF Antenna | 37 |
| 4.2 | Frequency Dependence of Anchor Heating | 39 |
| 5 | Effective Heating with Phase-Controlling | 43 |
| 5.1 | Concept of phase-control experiments | 43 |
| 5.2 | Phase-control experiments on GAMMA 10 | 44 |
| 5.3 | Anchor Heating in Phase-control Experiments | 45 |
| 5.4 | Wave Propagation in Phase-control Experiments | 49 |
| 5.5 | Producing High Density Plasmas with Phase-control | 51 |
| 6 | Wave Analysis by TASK/WF | 52 |
| 6.1 | Typical Excited Waves for Anchor Heating | 52 |
| 6.2 | Simulation of Phase-Control Experiments by GAMMA 10 Configuration | 53 |
| 6.2.1 | Effect of relative location of ICRF antennas and the resonance layer | 53 |
| 6.2.2 | Density dependence of Phase Control Experiments | 54 |
| 7 | Conclusion | 56 |

Chapter 1

Introduction

An energy resource issue is one of the most important problems in the world. As one possible solution to this problem, a electric power generated by using nuclear fusion is now under development [1]. The nuclear fusion is regarded as a next-generation energy, and the ultimate energy resource instead of fossil fuels and nuclear fission, because it has many advantages. The nuclear fusion can take fuel from seawater [2, 3, 4], has no danger of spiraling out of control, and releases no greenhouse effect gas in generation [5, 6]. The fusion energy gain factor indicating the ratio of the output energy for the input energy denotes Q . In order to use nuclear fusion as energy resource, it is necessary to achieve the self-ignition condition ($Q = \infty$). The nuclear fusion research progresses with many experimental devices [1]. There are two methods of devices. The magnetic confinement is one of the method, the confinement fuel by laser power is the another method. In the magnetic confinement systems, there are some types of experimental device. The research in the magnetic confinement systems progresses with the construction of the generation demonstration reactor in Tokamak [7, 8]. ITER [9, 10, 11], which is the largest Tokamak reactor, is the one of the most important project in the fusion research. ITER is in progress under the collaboration of China, EU, India, Japan, Korea, Russia, and United State, and in under construction at San-par-de Durance in France in 2015. For the feasibility demonstration by nuclear fusion on ITER, it needs to research about heating plasmas, controlling instabilities, plasma-wall interactions, and so on. There are some methods for heating plasmas in the magnetic confinement devices. Waves in Ion-Cyclotron Range of Frequency (ICRF) are used for ion-heating in magnetic confinements. In the magnetic fields, the ions are confirmed in the cyclotron motion. Equation 1.1 shows the cyclotron frequency.

$$\omega_{cs} = \frac{ZeB_0}{m_s} \quad (1.1)$$

where ω_{cs} , Z , e , B_0 , m_s , and s denote the cyclotron frequency, atomic value, electron charge, the magnetic field strength, mass of particle and the kinds of particles, respectively. For example, the cyclotron frequency of hydrogen with 1T in magnetic field strength is 15.24MHz. The ion-heating with ICRF waves is achieved by inputting waves in same frequency of the cyclotron frequency at the resonance layer.

GAMMA 10 is the largest tandem mirror device in the world [12, 13]. It has high temperature ions heated by ICRF wave. The magnetic field lines are open at the both ends. GAMMA 10 is categorized in the open ended systems. In the standard discharge, the ion temperature and electron density are achieved about $\sim 5\text{keV}$, and $\sim 10^{18}\text{m}^{-3}$, respectively. On GAMMA 10, the diverter simulation experiments progress with high temperature and open magnetic configuration [14, 15, 16, 17, 18, 19, 20, 21, 22, 23]. In this experiments, it is required to produce and control high temperature and high density plasmas. On GAMMA 10, ICRF waves are used for producing plasmas, heating ions, and keeping Magneto Hydro Dynamic (MHD) stability. In order to achieve producing high density plasmas more effectively, the enhancement of anchor heating using ICRF antenna installed in the anchor cell is introduced. Figure 1.1 shows the line-integrated density dependence of the particle flux the end of GAMMA 10. It is clearly observed that the relationship exists between increase of the particle flux and the line-integrated density. It is also indicated that the increase of

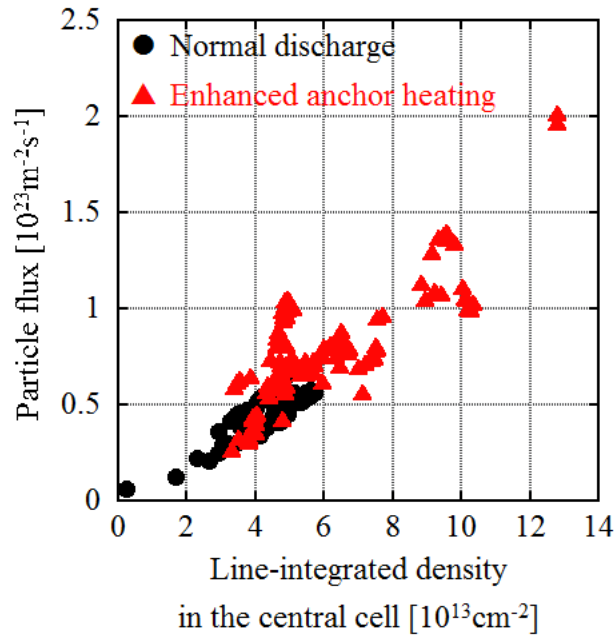


Figure 1.1 The line-integrated density dependence of the particle flux the end of GAMMA 10. It is clearly observed that the relationship exists increase of the particle flux is indicated with the increase

the particle flux is achieved by the enhancement of anchor heating.

In this thesis, the optimization of heating and controlling plasmas by enhancement of the anchor ICRF heating is discussed. In order to enhance ion-heating in the anchor cell, the phase-control experiments [24] is introduced. The phase-control experiments use wave interference of waves inputting by two ICRF antennas. In the phase-control experiments, it is clearly observed that the plasma parameters such as the line-integrated density in the central cell and the ion temperature in the anchor cell can be controlled and by phase-difference of antenna currents. In order to analyze wave propagation and the absorbed RF power in the anchor heating experiments, three dimensional full wave code, which is developed by A. Fukuyama at Kyoto University, is introduced. TASK/WF [25, 26] is the part of the integrated simulation code developing at the large scale experimental devices such as ITER and LHD [27, 28, 29, 30, 31, 32]. In the large scale experiments, plasma parameters, propagation of waves and performance of antennas are calculated by the

numerical simulation. In this thesis, the propagation of ICRF waves in the anchor heating experiments is calculated by TASK/WF. Because TASK/WF is three dimensional code, the wave propagation can be calculated in the minimum-B mirror configuration.

The contents of this thesis are as follows. The experimental setup is shown in chapter 2. The magnetic field of GAMMA 10, the heating system including ICRF antennas, and the diagnostics are presented. The waves in plasmas for ion-heating are presented in chapter 3. Three dimensional full wave code in order to analyze wave propagation is presented in chapter 4. The anchor heating experiments are presented in chapter 5. The phase-control experiments are discussed in chapter 6. The results of wave analysis by TASK/WF are also indicated. Chapter 7 summarizes the results of this thesis.

Chapter 2

Experimental Setup

2.1 Principle of confinement in the magnetic mirror

In the magnetic mirror configuration, we can consider the principle of confinement as following. The charged particles in the magnetic field follow the conservation of energy and the preservation of the magnetic moment.

$$E = \frac{m(v_{\parallel}^2 + v_{\perp}^2)}{2} + q\phi(z) = \text{const} \quad (2.1)$$

and

$$\mu \equiv \frac{mv_{\perp}^2}{2B(z)} = \text{const} \quad (2.2)$$

show the conservation of energy and the preservation of the magnetic moment, respectively. In the Equation (2.1) and (2.2), E , m , v_{\parallel} , v_{\perp} , q , $\phi(z)$, μ , $B(z)$ denote energy, mass of particle, velocity of parallel direction, velocity of vertical direction, electric charge, potential, magnetic moment, and magnetic field strength, respectively. When v_{\parallel} is zero, the particles are confined in the mirror configuration. From the Equation (2.1) and (2.2), we derive the condition of confinement of charge particles in magnetic mirror configuration.

$$v_{\perp}'^2 = v_{\parallel 0}^2 + v_{\perp 0}^2 = v_0^2 \quad (2.3)$$

and

$$\begin{aligned} \mu &= \frac{mv_{\perp 0}^2}{2B_0} = \frac{mv_{\perp}'^2}{2B'} \\ \frac{v_{\perp 0}^2}{B_0} &= \frac{v_{\perp}'^2}{B'} \end{aligned} \quad (2.4)$$

where $v_{\perp 0}$, B_0 , v_{\perp}' , and B' denote velocity of vertical direction and magnetic field strength in the mirror configuration, velocity of vertical direction and the magnetic field strength at the turning point. From Equation (2.3) and (2.4), we obtain the following relationship.

$$\frac{B_0}{B'} = \frac{v_{\perp 0}^2}{v_{\perp}'^2} = \frac{v_{\perp 0}^2}{v_0^2} \equiv \sin^2 \theta_t \quad (2.5)$$

where θ_t denotes the pitch angle in the velocity space in the mirror configuration. The charged particles of θ_t are reflected at the location of B' . We consider the minimum pitch angle to reflect in the mirror configuration. Replacing B' by B_M in the Equation (2.5), we see the smallest θ_M which can confine the particles. θ_M and B_M denote the pitch angle and magnetic field strength at the mirror throat, at which is

the maxim magnetic field strength.

$$\sin^2 \theta_M = \frac{B_0}{B_M} \equiv \frac{1}{R} \quad (2.6)$$

where R denotes the mirror ratio. According to Equation (2.6), there are the boundary in the velocity space, which called a loss cone.

2.2 The GAMMA10 tandem mirror device

2.2.1 Magnetic Mirror Configuration on GAMMA 10

Figure 2.1 shows the schematic drawing of (a) the simple mirror configuration and (b) a minimum-B mirror configuration produced by baseball coil. On GAMMA 10, the central cell and the plug/barrier cells are the simple magnetic mirror configurations and the anchor cell is a minimum-B mirror configuration. The magnetic lines in a minimum-B mirror configuration are convex towards the midpoint. The magnetic field strength increases towards outside from midpoint as shown in Fig. 2.1(b). On GAMMA 10, the mirror ratio as shown in Equation 2.6 of the central cell is 5, that of the anchor cell is 3.

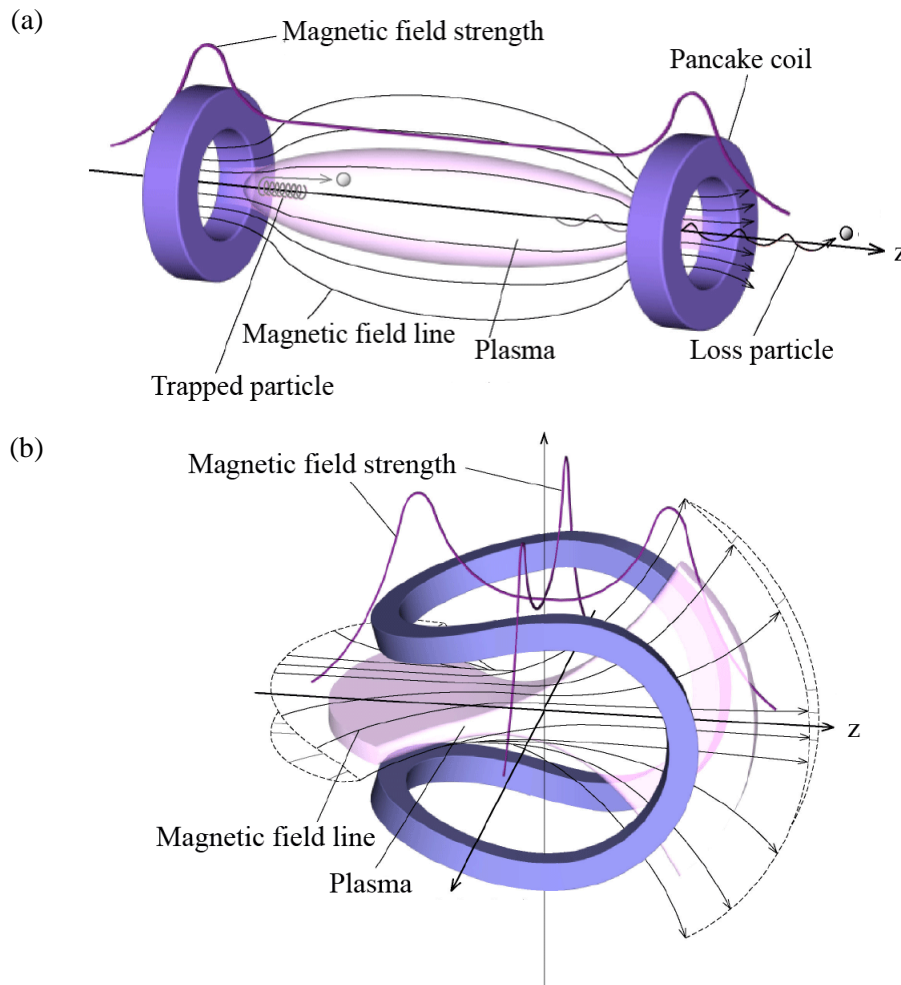


Figure 2.1 Schematic drawing of (a) simple mirror configuration produced by the pair of two coils, and (b) minimum-B mirror configuration produced by baseball coil.

2.2.2 Configuration of GAMMA 10

GAMMA 10, the largest tandem mirror device in the world, consists five mirror configurations. Figure

2.2 shows the schematic drawing of the GAMMA 10 tandem mirror device. This figure shows the vacuum vessel, coil configurations, five mirror configurations, the profile of the magnetic field strength on z axis, and the location of ICRF antennas. A central cell is a main confinement region. Two quadrupole minimum-B anchor cells are connected to each sides of the central cell for keeping MHD stabilization. Two plug/barrier cells are connected to next to the anchor cells. On GAMMA 10, a magnetic field is produced by pancake coils, race-track coils and baseball coils. The central cell is the simple magnetic mirror produced by pancake coils, 0.4T in magnetic field strength at midplane, and 5.6m in length. The anchor cells are the minimum-B mirror configurations produced by baseball coils, 0.61T in magnetic field strength at the midpoint, and 1.6m in length. GAMMA 10 is 27m in length and 180m^{-3} of vacuum vessel.

The positive potential is produced by high temperature plasmas in the magnetic mirror. These potential are used for the enhancement of confinement plasmas in the main confinement region on tandem mirror device. On GAMMA 10, there are five magnetic mirror configurations as shown in Fig. 2.2. On GAMMA 10, there are some methods for producing the potential for the enhancement of confinement plasmas in the central cell on GAMMA 10. The injecting waves in electron cyclotron range of frequency in the plug/barrier cell is a one of the method [33]. The injecting neutral beam in the plug/barrier cell [34] and the producing pressure plasmas in the anchor cell are another methods.

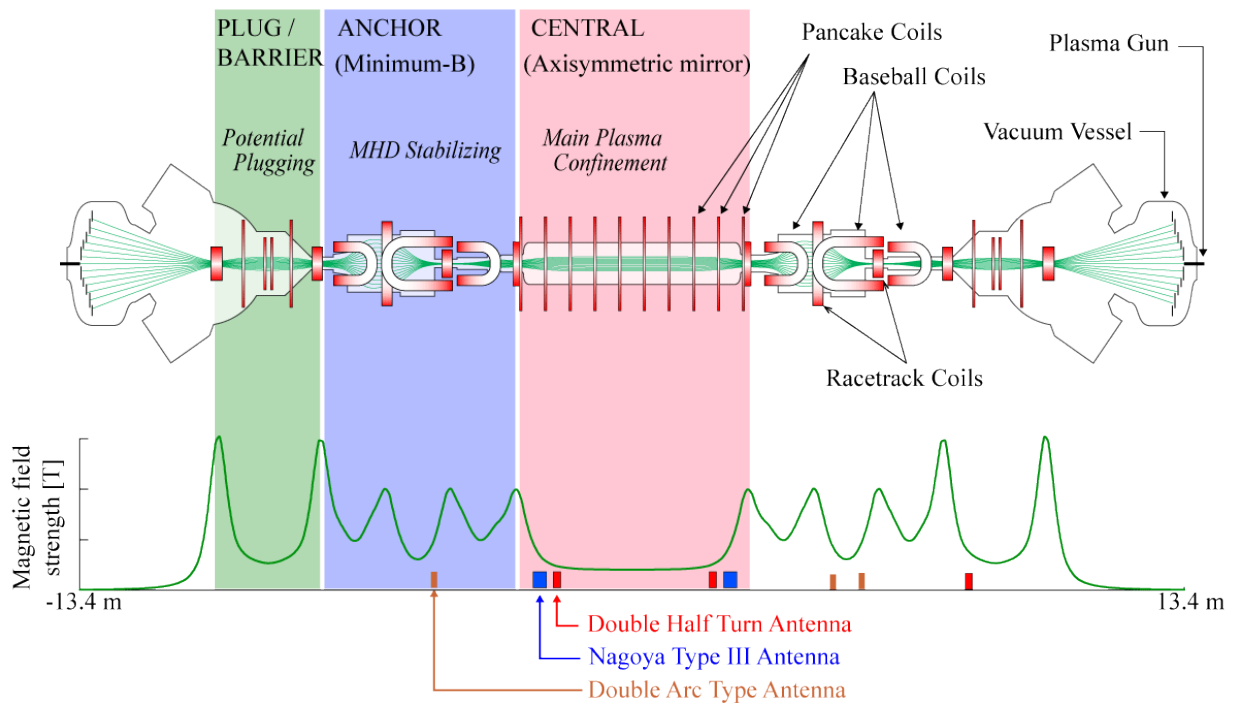


Figure 2.2 Schematic drawing of the GAMMA 10 tandem mirror device. This figure shows the vacuum vessel, coil configurations, the profile of the magnetic field strength, and the location of ICRF antennas.

2.2.3 Gas Fueling System and Plasma Gun

Figure 2.3 shows the schematic drawing of gas puffing system in the west side of the central cell. Table 2.1 shows the location and shape of gas injector of gas puffing systems. The hydrogen gas which is controlled by the electric-piezo valve is injected from the gas fueling systems located as shown in Fig. 2.3, and Table 2.1. In the standard discharge, two gas fueling systems, which are called GP(#1b, #2b), and GP(#3, #4), are used. GP(#2b) and GP(#4) are installed at the west side of the central cell.

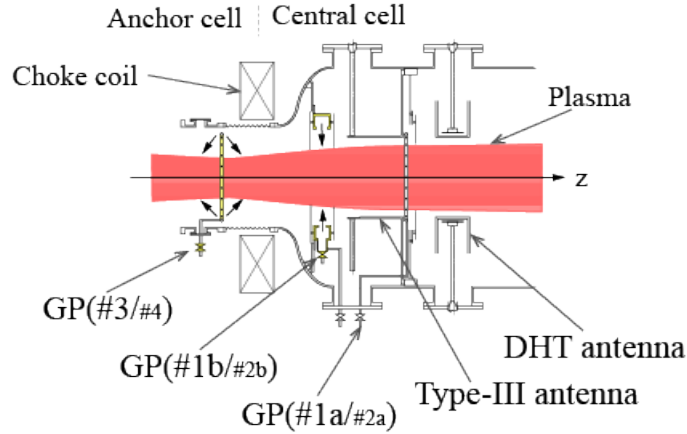


Figure 2.3 Schematic drawing of gas puffing system in the east end of the central cell

| Label of GP | Location [m] | Shape of gas puffing system |
|-------------|--------------|-----------------------------|
| GP1a | -2.052 | Gas box |
| GP1b | -2.500 | Gas ring |
| GP2a | 2.052 | Gas box |
| GP2b | 2.500 | Gas ring |
| GP3a | -3.0 | Gas ring |
| GP4a | 3.0 | Gas ring |
| GP5 | -8.8 | Nozzle |
| GP6 | 8.8 | Gas ring |
| GP7 | 0.2 | Nozzle |

Table 2.1 The location and shape of gas puffing systems on GAMMA 10

The starting of discharge on GAMMA 10 is carried out by plasmas injection by Magneto Plasma Dynamic Arcjet (MPDA) plasma gun at the both ends of GAMMA 10. Figure 2.4 shows Schematic drawing of MPDA plasma gun. The plasma produced in the MPDA is accelerated by the Lorentz force.

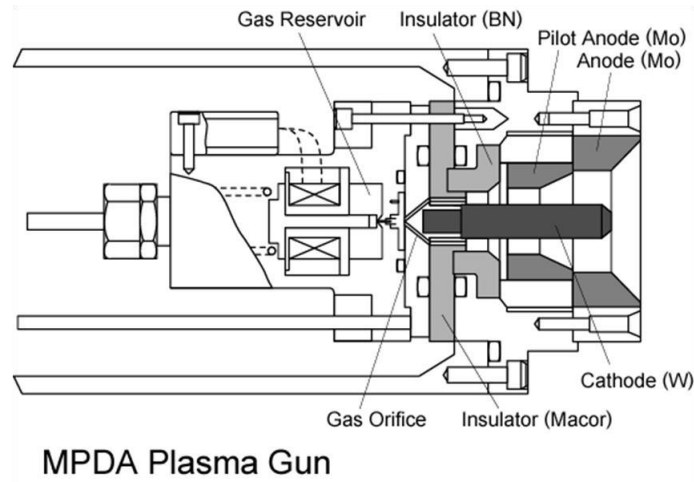


Figure 2.4 Schematic drawing of MPDA plasma gun which are installed at the both ends.

2.2.4 Electron Cyclotron Resonance Heating and Neutral Beam Injection systems

On GAMMA 10, other heating systems are installed. Table 2.2 shows (a) performances of Electron Cyclotron Resonance Heating (ECRH) systems, and (b) performances of Neutral Beam Injection (NBI) systems on GAMMA 10. There are five ECRH systems [14] and seven NBI systems [34].

| | | | | | | |
|-----|-------|--------------------|--|-----------------------------------|--------------------------|---------------------------|
| (a) | | Frequency [GHz] | Location of heating [m] (Magnetic field strength) | | Maxim Output Power | |
| | c-ECH | 28 | 2.43 (1T) | | 500kW | |
| | p-ECH | 28 | ± 9.62 (1T) | | $500\text{kW} \times 2$ | |
| | b-ECH | 28 | ± 8.90 (0.5T) | | $200\text{kW} \times 2$ | |
| (b) | | Energy [keV] | Location of injection [m] | Current [A] \times Beam Line | Incidence angle [deg] | Divergence angle [deg] |
| | c-NBI | 25 | -1.23 | 30×1 | 90 | 1.0 |
| | a-NBI | 25 | ± 5.20 | 60×2 | 82 | 1.2 |
| | s-NBI | 25 | ± 8.70 | 60×2 | 41 | 1.2 |
| | p-NBI | 25 | ± 8.70 | 60×2 | 30 | 1.2 |

Table 2.2 (a)Frequency and location of heating and maxim output power of ECRH system and the locations and maxim output power of NBI system on GAMMA 10

2.3 Ion Cyclotron Range of Frequency (ICRF) Heating

2.3.1 ICRF Systems

On GAMMA10, the three ICRF systems including five amplifiers, which are named RF1(PA1, PA2), RF2(PA3, PA4), and RF3, are used for producing plasmas, heating ions, and keeping MHD stability. The table 2.3 shows the frequency range and the maxim output power of each system.

| | Frequency Range | Maximum Output Power |
|---------------|-----------------|----------------------|
| RF1(PA1, PA2) | 7.5~15 MHz | 300kW \times 0.5ms |
| RF2(PA3, PA4) | 4.4~9.6 MHz | 300kW \times 0.5ms |
| RF3 | 4~10 MHz | 200kW \times 0.5ms |

Table 2.3 The frequency range and maximum output power of ICRF system on GAMMA 10

2.3.2 ICRF Antennas

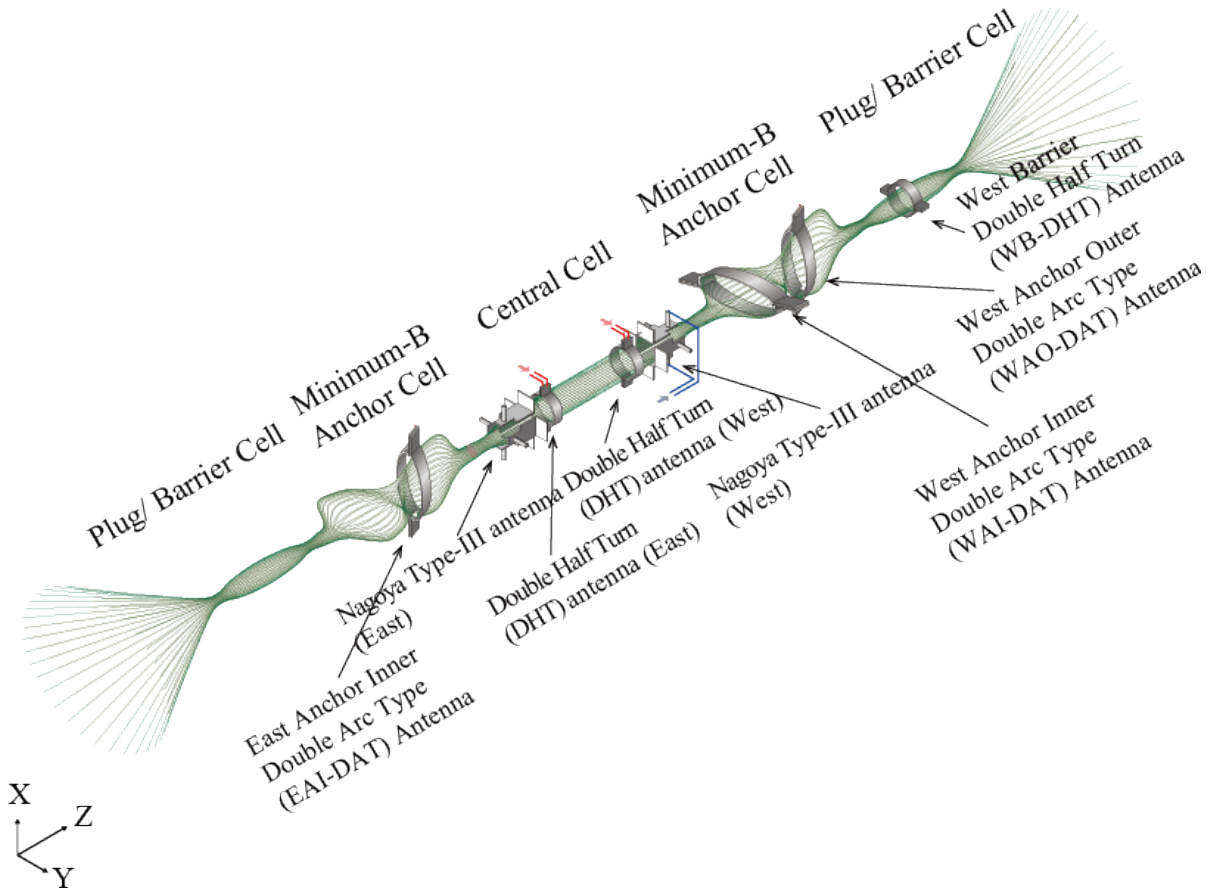


Figure 2.5 Schematic drawing of magnetic field lines of GAMMA 10. This figure also shows the location of the central cell, minimum-B anchor cells, and plug/barrier cells, and the configuration of ICRF antennas. There are eight sets of ICRF antennas.

The eight sets of ICRF antennas are installed. Figure 2.5 shows the schematic drawing of magnetic field lines of GAMMA 10. The location of the central cell, minimum-B anchor cells, and plug/barrier cells, and the configuration of ICRF antennas are also indicated. Here, the origin $(x, y, z) = (0, 0, 0)$ of GAMMA 10 is defined at the midpoint of the central cell, and x-axis, y-axis and z-axis are defined as shown in Fig. 2.5. There are three kinds of antennas. Nagoya Type-III antennas [24] are installed at both ends of the central cell ($z = \pm 2.2\text{m}$). The antenna current of Type-III antenna flows in the parallel direction to the magnetic field lines. The three sets of Double Half Turn (DHT) antennas are installed in the central cell ($z = \pm 1.7\text{m}$) and at the west plug/barrier cell ($z = 8.4\text{m}$). The three Double Arc Type (DAT) antennas [35, 36] are installed in the anchor cell. Figure 2.6 shows the picture of (a) Type-III antenna and DHT antenna at the west side of the central cell, and (b) WAI-DAT and WAO-DAT antennas in the west anchor cell. One set of DAT antennas is in the east anchor cell ($z = -4.93\text{m}$), called EAI-DAT, and two sets of DAT antennas are in the west anchor cell. In the west anchor cell, the DAT antenna located near the central ($z = 4.93\text{m}$) cell is called WAI-DAT, and another ($z = 5.47\text{m}$) is WAO-DAT as shown in Fig. 2.6. The antenna current of DHT and DAT antennas flows in the perpendicular direction of the magnetic field lines.

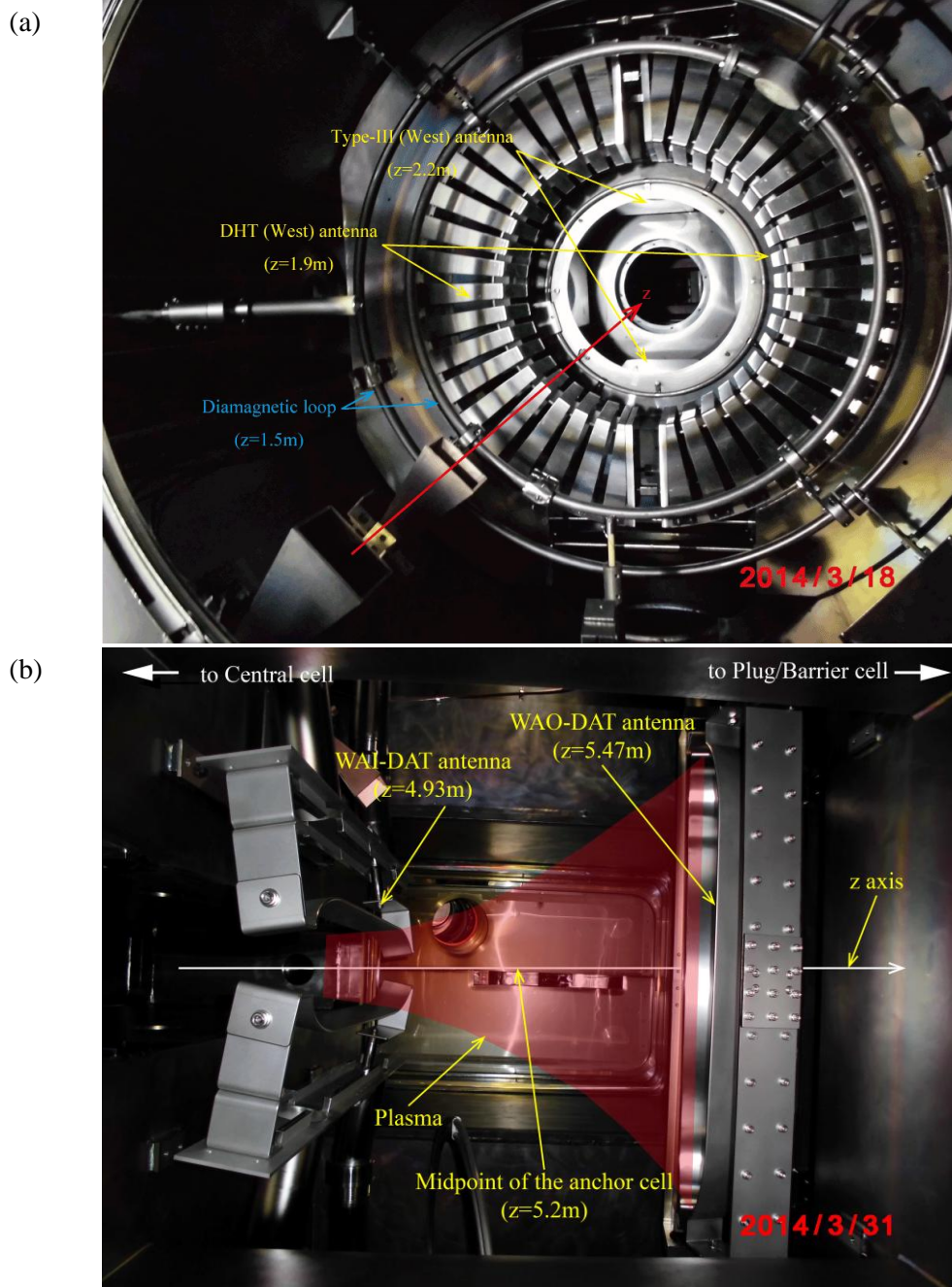


Figure 2.6 Photographs of (a) Type-III antenna and DHT antenna at the west side of the central cell, and (b) WAI-DAT and WAO-DAT antennas in the west anchor cell.

Figure 2.7 shows ω/Ω_{ci} value along the z-axis in GAMMA 10. The resonance layer of 6.36MHz waves exists in the central cell, and the resonance layers of 9.7MHz, 9.9MHz, and 10.3MHz exist in the both anchor cells as shown in Fig. 2.7. Here, ω is defined as the applied frequency. In the standard operation, the injection of short pulse (1ms plasma) from MPDA plasma gun [37] at the end starts discharge, and ICRF powers are applied by Type-III antennas with RF1 which excites 9.9MHz or 10.3MHz waves for the fundamental ion cyclotron resonance heating at the midplane in the anchor cell [38, 39], and DHT antennas in the central cell with RF2 which excites 6.36MHz waves for ion-heating in the central cell, with the hydrogen gas puffing. In order to avoid the interference between the east and west Type-III antennas, the different frequencies (9.9MHz and 10.3MHz) are chosen in the east and west sides. Table 2.4 shows the location and applied frequency of ICRF antennas.

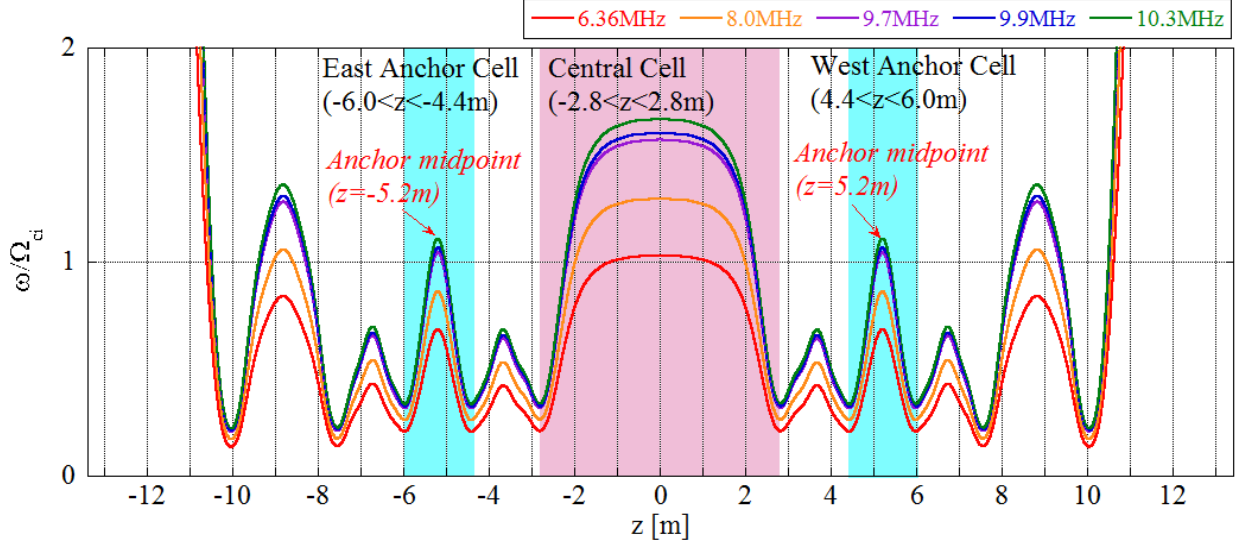


Figure 2.7 ω/Ω_{ci} value on GAMMA 10. The resonance layer of 6.36MHz waves exists in the central cell, and the resonance layers of 9.7MHz, 9.9MHz, and 10.3MHz exist in the both anchor cells.

| Antenna | Location of antenna [m] | Applied frequency [MHz] |
|---|-------------------------|-------------------------|
| East Anchor Inner Double Arc Type (EAI-DAT) | -4.925 | 9.7MHz |
| | | 9.9MHz |
| Nagoya Type-III antenna (East) | -2.315 | 9.9MHz |
| Double Half Turn (East) | -1.900 | 6.36MHz |
| Double Half Turn (West) | 1.900 | 6.36MHz |
| Nagoya Type-III antenna (West) | 2.315 | 10.3MHz |
| West Anchor Inner Double Arc Type (WAI-DAT) | 4.925 | 9.7MHz |
| | | 10.3MHz |
| West Anchor Outer Double Arc Type (WAO-DAT) | 5.475 | 7.7MHz, 8.0MHz, 8.5MHz |
| | | 9.7MHz |
| | | 10.3MHz |
| West Barrier Double Half Turn | 8.420 | 8.0MHz, 8.5MHz, 10.3MHz |

Table 2.4 Location and applied frequency of ICRF antennas on GAMMA 10. There are two sets of Type-III antennas, three sets of DHT antennas, and three sets of DAT antennas on GAMMA 10.

2.3.2 Anchor Heating for Magneto-Hydro Dynamic (MHD) stabilization

On GAMMA 10, plasmas are confined by magnetic mirror configuration. In order to confine high pressure plasmas stably, it is important to keep the Magneto-Hydro Dynamic (MHD) stabilization. High pressure plasmas in the anchor cell is required for MHD stabilization. In standard discharge, 9.9MHz or 10.3MHz ICRF waves excited Type-III antennas with mode-conversion are used for ion-heating in the anchor cell. Figure 2.8 shows the schematic drawing of the contour map of the magnetic field strength in the anchor cell on x-z plane ($y=0$). Figure 2.9 shows the data points of stably maintained diamagnetism of the central cell and anchor cell. The magnetic field lines of $R_{cc}=0.18m$ is also indicated with dashed lines in Fig. 2.8. Here, R_{cc} denotes the conversion radius at the midpoint of the central cell ($z=0m$). In the anchor cell, there is closed magnetic surface near the midpoint of the anchor cell. In order to heat ions at the closed resonance layer, the frequency of ICRF waves is restricted near 10MHz. From Fig 2.9, it is clear that high pressure plasmas in the anchor cell is necessary for keeping high pressure plasmas in the central cell [40, 41, 42].

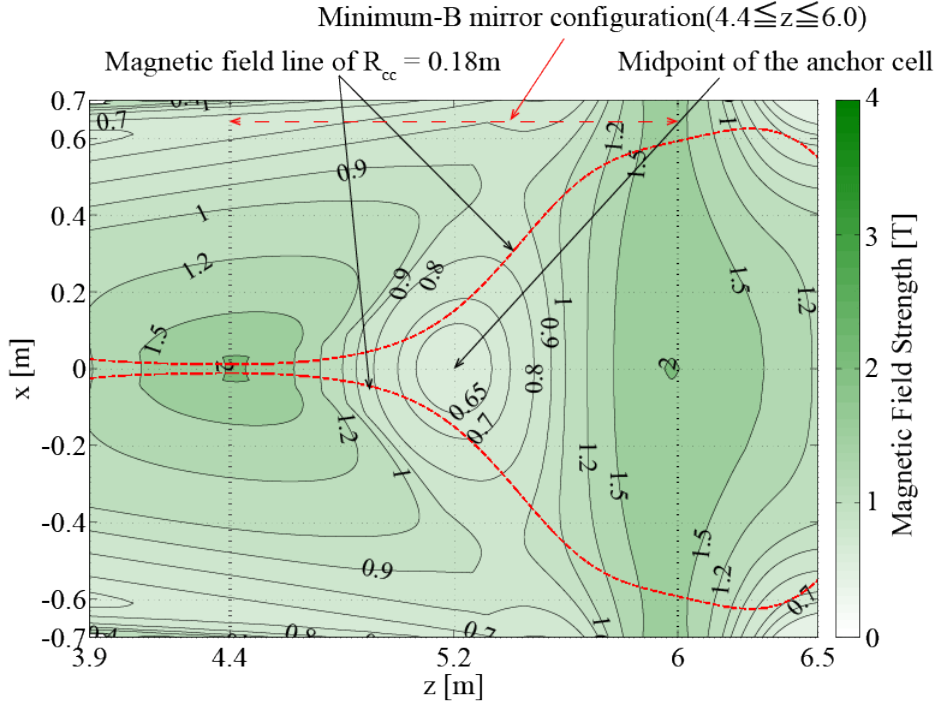


Figure 2.8 Schematic drawing of the contour map of the magnetic field strength in the anchor cell. The magnetic field lines of $R_{cc}=0.18m$ is also indicated.

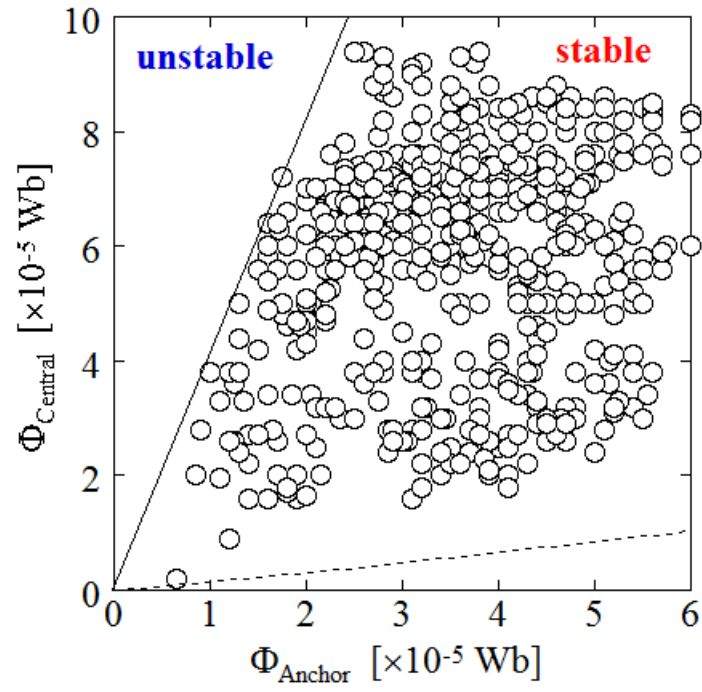


Figure 2.9 The data points of diamagnetism of the central cell and anchor cell.

2.4 Diagnostics

On GAMMA10, plasma parameters such as pressure, line-integrated density of electrons, and ion temperature are measured.. Figure 2.10 shows the magnetic field strength along the z-axis and the location of diagnostics.

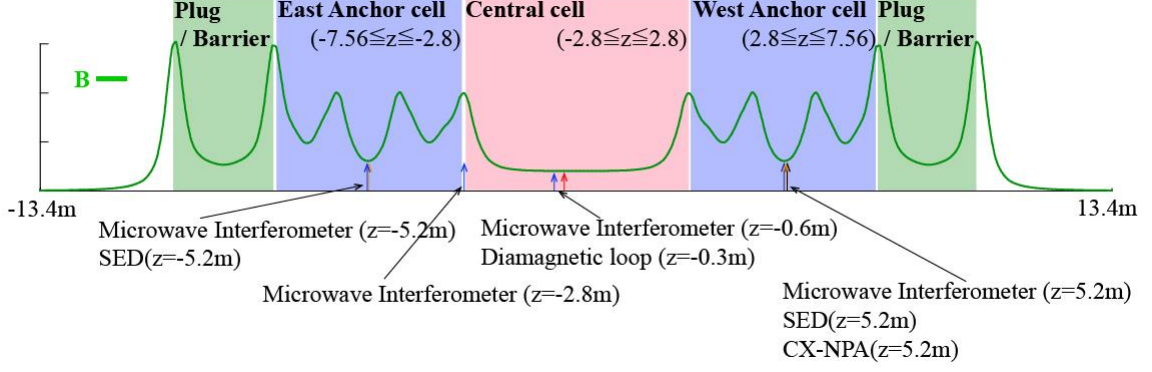


Figure 2.10 Schematic drawing of the magnetic field strength on z axis and location of diagnostics.

2.4.1 Measurement Instruments for ICRF Heating

2.4.1.1 Secondary Electron Detector

The secondary electron detector (SED) is installed at the midpoint of the anchor cell ($z = \pm 5.2\text{m}$). It measures the charge-exchanged neutrals, which has the information of the energy at the midpoint of the anchor cell. The current value of SED is shown as

$$I_{\text{SED}} = en_0n_i\langle\sigma v\rangle_{\text{CX}}\frac{\Delta\Omega}{4\pi}\Delta V_p\int_0^\infty f_i(E)\gamma(E)dE \quad (2.7)$$

where n_0 , n_i , $\langle\sigma v\rangle_{\text{CX}}$, $\Delta\Omega$, ΔV_p , $f_i(E)$, and $\gamma(E)$ denote the density of the hydrogen neutral, the density of ions, the reaction rate of charge exchange, solid angle, the plasma volume in range of vision of detector, the ion energy distribution function, and the secondary electron emission coefficient, respectively. Figure 2.11 shows the schematic drawing of (a) Secondary Electron Detector (SED) and (b) circuit model of SED, and photographs of (c) SED and (d) the target metal. Here, the solid angle of the SED is decided by the relationship of the length of collector and the metal target. The SED is set as including the midpoint of the anchor cell. If high-speed neutral particle collides with the target plate which is biased in positive voltage, the secondary electrons are emitted from the target plate and trapped by the collector plate. The energy in the anchor cell is evaluated by the current created by secondary electrons.

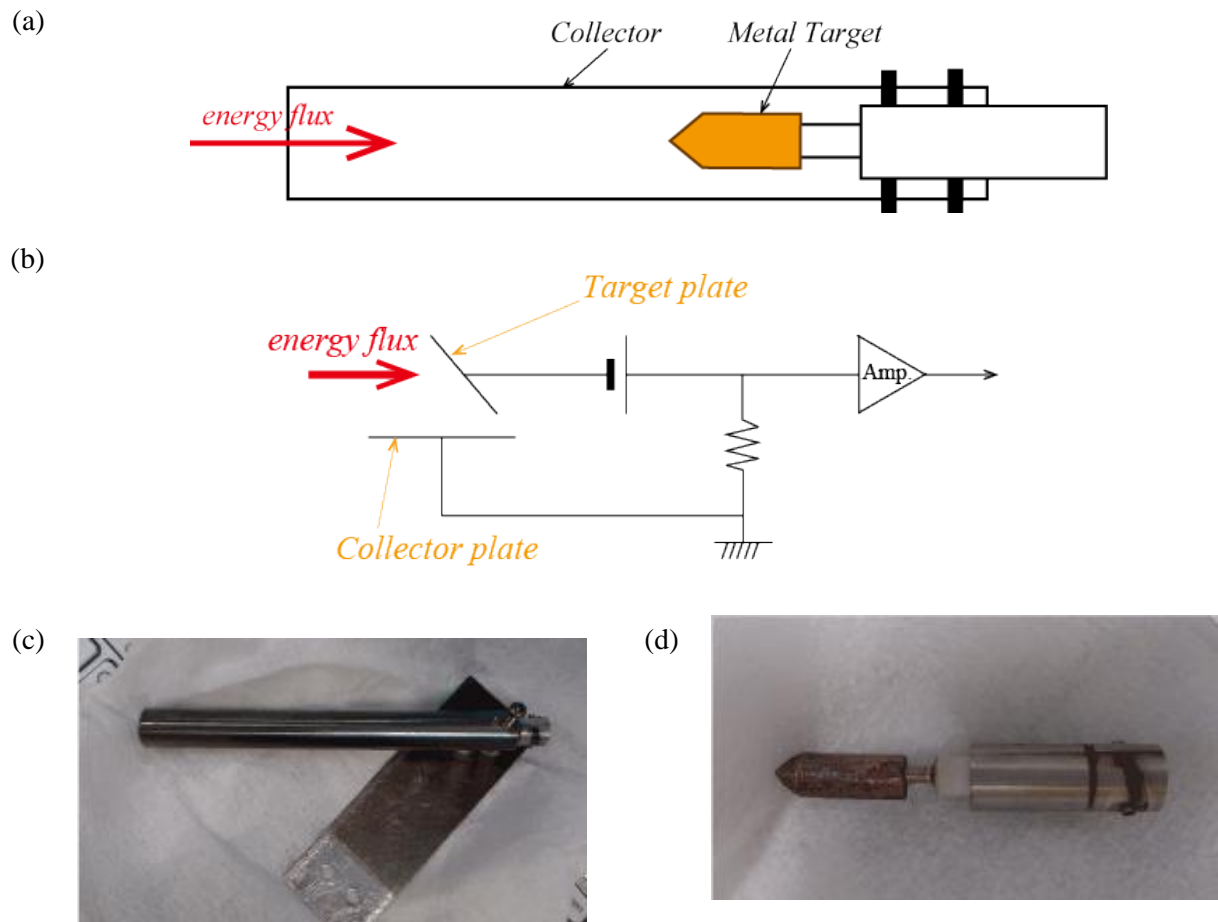


Figure 2.11 Schematic drawing of (a) Secondary Electron Detector (SED) and (b) circuit model of SED, and photographs of (c) SED and (d) the target metal.

2.4.1.2 Current pick-up coils

In order to measure antenna current, single pick-up coils are installed near the ICRF antennas. The single coil picks up the oscillating the magnetic flux created by antenna current, according to a Ampere law. Figure 2.12 shows the photograph of the current pick-up coil. The single coil is installed at near the antenna current as shown in Fig 2.12. It is used for measuring the phase difference of antenna current in the phase control experiments, and the antenna loading as shown in following section.

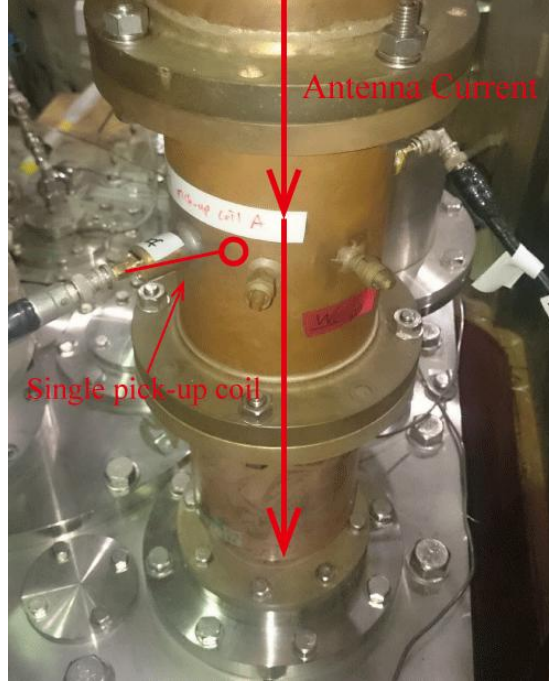


Figure 2.12 Photograph of the current pick-up coil. The single coil is installed at near the antenna current.

2.4.1.3 Measurement of ICRF power

Figure 2.13 shows the circuit model of measurement of ICRF power and antenna loading. In the experiments, the input power, the radiated power, and the antenna loading are measured in following method. The power output by an oscillator is defined as the forward power, and the power reflected by ICRF antenna to the oscillator is defined as the reflected power as shown in Fig. 2.13.

$$P_{in} = P_{fwd} - P_{ref} \quad (2.8)$$

where P_{in} , P_{fwd} , and P_{ref} denote the input power, the forward power, and the reflected power. The forward and reflected power are measured with the directional coupler. The input power is estimated in Equation (2.9). The input power includes the absorbed power in the circuit and the radiated power to the plasmas. The input power is absorbed with the resistance components. The symbols of r_{circ} , and r_{plasma} denote the resistance component of the circuit and plasma, respectively. In order to calculate r_{circ} , the ICRF power are inputted to the circuit without plasmas. This discharge is called the pre-pulse. r_{circ} is calculated from the pre-pulse as Equation (2.9). In the pre-pulse, we can consider that all of the power is absorbed in the circuit, because there is no plasma resistance.

$$P_{in} = P_{fwd} - P_{ref} \quad (2.9)$$

$$= \frac{1}{2} \cdot r_{circ} \cdot I_{circ}^2 = P_{circ}$$

where I_{circ} denote the antenna current in circuit measured by the single pick-up coil. The following equation shows the method of calculation with plasma.

$$\begin{aligned} P_{in} &= P_{inc} - P_{ref} \\ &= P_{circ} + P_{net} \\ &= \frac{1}{2} (r_{circ} + r_{plasma}) I_{circ}^2 \end{aligned} \quad (2.10)$$

where r_{plasma} denotes the plasma resistance. In Equation (2.10), P_{inc} , P_{ref} , and I_{circ} are measured. The radiated power is denoted by P_{net} . From Equation (2.10),

$$P_{net} = P_{in} - \frac{1}{2} r_{circ} I_{circ}^2 \quad (2.11)$$

The ratio of P_{net} and P_{in} is so-called the antenna loading. The antenna loading is calculated as following.

$$\begin{aligned} \text{Antenna Loading} &= \frac{P_{net}}{P_{in}} \\ &= \frac{P_{net}}{P_{net} + P_{plasma}} \\ &= \frac{r_{net}}{r_{net} + r_{plasma}} \end{aligned} \quad (2.12)$$

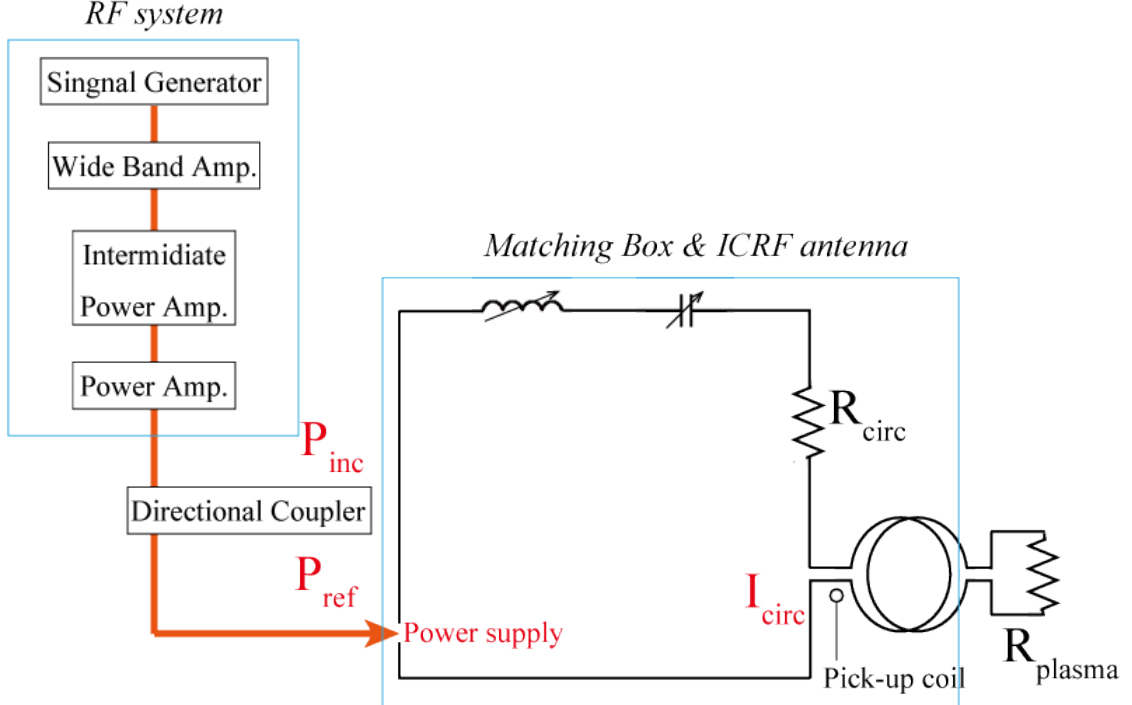


Figure 2.13 Schematic drawing of the circuit model of ICRF

2.4.2 Fundamental Measurement Instruments

2.4.2.1 Diamagnetic loop

The diamagnetic loops are installed for measuring pressure of plasmas in the central cell [43]. The plasma has a property to remove internal magnetic flux for a diamagnetic effect. Plasma pressure can be estimated from the diamagnetic signals. A simple model for estimating the plasma pressure is shown as follows. The equation of plasma pressure is described by the ideal MHD equation.

$$\rho \frac{\partial \mathbf{v}}{\partial t} = \mathbf{j} \times \mathbf{B} - \nabla \mathbf{p} \quad (2.13)$$

$$\begin{aligned} \rho &= n_i m_i + n_e m_e \sim n(m_i + m_e) \\ \mathbf{v} &= \frac{n_i m_i \mathbf{v}_i + n_e m_e \mathbf{v}_e}{\rho} \end{aligned} \quad (2.14)$$

$$\mathbf{j} = e(n_i \mathbf{v}_i - n_e \mathbf{v}_e) = en(\mathbf{v}_i - \mathbf{v}_e)$$

where ρ , \mathbf{v} , \mathbf{j} , \mathbf{B} , \mathbf{p} , n_i , n_e and n denote mass density, velocity, current, magnetic field strength, plasma pressure, the density of ions, the density of electrons, and the density of plasmas, respectively. \mathbf{v}_i and \mathbf{v}_e are the velocity of ions and electrons respectively. In the steady state condition, $\partial/\partial t = 0$, from Equation (2.13),

$$0 = \mathbf{j} \times \mathbf{B} - \nabla \mathbf{p} \quad (2.15)$$

From the Maxwell's equation of $\nabla \times \mathbf{B} = \mu_0 \mathbf{j}$. μ_0 denote the magnetic permeability of vacuum. Equation (2.15) is represented as

$$\nabla \mathbf{p} = \left(\frac{1}{\mu_0} \times \mathbf{B} \right) \times \mathbf{B} \quad (2.16)$$

The right-hand side of equation (2.16) can be described by

$$\begin{aligned} \left(\frac{1}{\mu_0} \times \mathbf{B} \right) \times \mathbf{B} &= \frac{1}{\mu_0} [-\nabla(\mathbf{B} \cdot \mathbf{B}) + 2(\mathbf{B} \cdot \nabla)\mathbf{B} + \mathbf{B} \times (\nabla \times \mathbf{B})] \\ (\nabla \times \mathbf{B}) \times \mathbf{B} &= (\mathbf{B} \cdot \nabla)\mathbf{B} - \frac{\nabla B^2}{2} \end{aligned} \quad (2.17)$$

Then equation (2.17) becomes

$$\nabla \left(\mathbf{p} + \frac{B^2}{2\mu_0} \right) = \frac{1}{\mu_0} (\mathbf{B} \cdot \nabla)\mathbf{B} . \quad (2.18)$$

In case of the plasma which is long to the z-direction, the right-hand side of Equation (2.18) is neglected and $B \gg B_r, B_\theta$ will be arranged. The equation about the pressure equilibrium are

$$p + \frac{B^2}{2\mu_0} = \text{const} . \quad (2.19)$$

From equation (2.19), the pressure in a straight cylindrical plasmas is obtains as following.

$$p = \frac{1}{2\mu_0} (B_0^2 - B^2) \quad (2.20)$$

where B_0 and B denote the magnetic field strength in the outside and inside of plasma, respectively. When

the plasma pressure is small, the plasma pressure can be obtained approximately.

$$p = \frac{B_0 \cdot \Delta B}{\mu_0} \quad (2.21)$$

$$\Delta B = B_0 - B$$

Figure 2.14 shows the schematic drawing of diamagnetic loop system in GAMMA 10. The diamagnetic loop systems consist a concentric pair of loops to improve the signal/noise ratio as shown in Fig. 2.9. The noise cancellation method works as follow. The magnetic flux measured by outer and inner loops, which are denoted by Φ_o and Φ_i , are simply written as follows.

$$\begin{aligned} \Phi_o &= \pi r_{plasma}^2 \cdot B + \pi(r_o^2 - r_{plasma}^2) \cdot B_0 \\ \Phi_i &= \pi r_{plasma}^2 \cdot B + \pi(r_i^2 - r_{plasma}^2) \cdot B_0 \end{aligned} \quad (2.22)$$

where r_{plasma} , r_o , and r_i denote the radii of plasmas, outer loop, and inner loop, respectively. The electromotive force generated on the loops is follows.

$$\begin{aligned} V_o &= -N \frac{\partial \Phi_o}{\partial t} = N\pi r_{plasma}^2 \frac{d}{dt}(\Delta B) - N\pi r_o^2 \frac{d}{dt}(B_0) \\ V_i &= -N \frac{\partial \Phi_i}{\partial t} = N\pi r_{plasma}^2 \frac{d}{dt}(\Delta B) - N\pi r_i^2 \frac{d}{dt}(B_0) \end{aligned} \quad (2.23)$$

where N denote the number of turns of each coil. In equation (2.23), the first term is the diamagnetic signal and the second term is noise signal due to the ripple of the magnetic field. The noise signal can be cancel using these concentric loops. The diamagnetic signal can be written as follow.

$$V \equiv N\pi r_{plasma}^2 \frac{d}{dt}(\Delta B) = V_i - \frac{r_i^2}{r_o^2 - r_i^2} (V_o^2 - V_i^2) \quad (2.24)$$

where V denote the ripple-cancelled loop signal. The diamagnetism, shown by W , is obtained from the time integration as follow.

$$W = N\pi r_{plasma}^2 (\Delta B) = \frac{1}{N} \int V dt \quad (2.25)$$

The substitution of Equation (2.20) into Equation (2.24) yields

$$p = \frac{B_0}{N\pi\mu_0 r_{plasma}^2} \int V dt = \frac{B_0}{N\pi r_{plasma}^2} W \quad (2.26)$$

Table 2.5 shows the location of the diamagnetic loops and the number of turns.

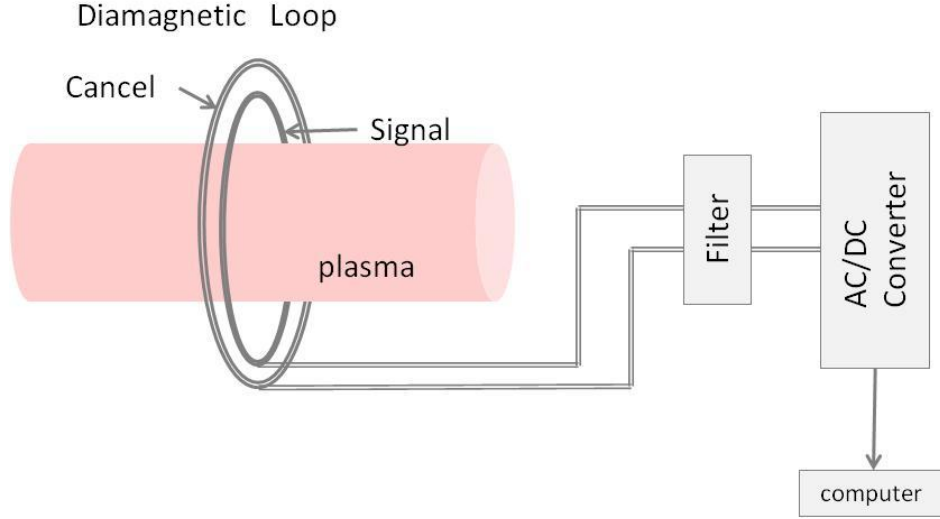


Figure 2.14 The schematic drawing of the diamagnetic loops

| | Location of z axis [m] | turns |
|--|------------------------|-------|
| DMCC(Diamagnetic loop at Central Cell) | -0.33 | 10 |
| DMCE(Diamagnetic loop at Central East) | -1.5 | 10 |
| DMCW(Diamagnetic loop at Central West) | 1.5 | 10 |
| DMCW2(Diamagnetic loop at Central West2) | 1.95 | 20 |
| DMEA(Diamagnetic loop at East Anchor) | -5.2 | 20 |
| DMWA(Diamagnetic loop at West Anchor) | 5.2 | 20 |

Table 2.5 The location of the diamagnetic loops and the number of turns

2.4.2.2 Microwave Interferometer

The line-integrated density is measured by the microwave interferometer. Figure 2.15 shows the schematic drawing of the interferometer installed in GAMMA 10. An O-mode is used for this measurement, because it has no dependence on the magnetic field. The mechanism of microwave interferometer is shown as follow. It doesn't depend in the magnetic field.

$$\varepsilon = 1 - \frac{\omega_p^2}{\omega^2} = 1 - \frac{n_e e^2}{\varepsilon_0 m_e \omega^2} \quad (2.27)$$

where ε , ω_p , ω , n_e , m_e , and ε_0 denote the relative permittivity of plasma, plasma frequency, frequency of microwave, electron density, electron mass, and relative permittivity of vacuum, respectively. When ω is larger than ω_p enough ($\omega \gg \omega_p$) with the positive relative permittivity of plasma ($\varepsilon > 0$), the wave length of microwave are written as

$$\lambda = \frac{\lambda_0}{\sqrt{\varepsilon}} = \frac{2\pi c}{\omega \sqrt{\varepsilon}}. \quad (2.28)$$

The measurement is performed by determining phase difference between microwave propagating inside and outside of plasmas as shown in Figure 2.15 The wave propagating inside the plasma is called as a

transmission wave, and the wave propagating only outside the plasma is called a reference wave. Phase difference ($\Delta\phi$) between the transmission wave and the reference wave is written as,

$$\Delta\phi = 2\pi \int_{-a}^a \left(\frac{1}{\lambda_0} - \frac{1}{\lambda} \right) dx \quad (2.29)$$

where λ_0 , λ and a denote the wave length of reference wave, the wave length transmission wave, and the radii of plasma. The substitution of Equation (2.29) with Equation (2.27) and (2.28) is written as,

$$\begin{aligned} \Delta\phi &= \frac{2\pi}{\lambda_0} \int_{-a}^a (1 - \sqrt{\epsilon}) dx \\ &= \frac{2\pi}{\lambda_0} \int_{-a}^a \left\{ 1 - \left(1 - \frac{n_e e^2}{2\epsilon_0 m_e \omega^2} \right) \right\} dx \\ &= \frac{\pi e^2}{\epsilon_0 m_e \lambda_0 \omega^2} \int_{-a}^a n_e(x) dx \end{aligned} \quad (2.30)$$

Table 2.6 shows the location, plasma radius at the measuring location of the microwave interferometer systems on GAMMA 10. The microwave in 70GHz is used for measurement, so the limit of density is calculated as $\sim 7.8 \times 10^{19} \text{m}^{-3}$.

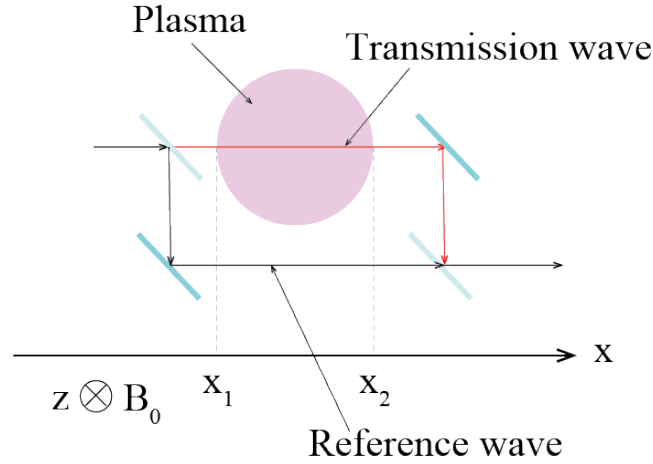


Figure 2.15 Schematic drawing of the microwave interferometer. The red line indicates the transmission wave and the black line indicates the reference wave.

| | Location of z axis [m] | Radius of plasmas[m] |
|------------|------------------------|----------------------|
| NLEP | -9.675 | 0.108 |
| NLEB | -8.66 | 0.162 |
| NLEA | -5.2 | 0.153 |
| NLCT | -2.8 | 0.081 |
| NLCC | -0.6 | 0.18 |
| NLCC-multi | 0 | 0.18 |
| NLWA | 5.2 | 0.153 |
| NLWB | 8.62 | 0.162 |
| NLWP | 9.690 | 0.108 |

Table 2.6 Location of microwave system for measuring the line-integrated density and the radius of plasmas

2.4.2.3 CX-NPA

In order to measure the ion temperature, the Charge eXchange Neutral Particle Analyzer (CA-NPA) is installed at the anchor cell ($z = \pm 5.2\text{m}$).

2.4.2.4 Electrostatic Probe and Segment Limiter

ElectroStatic Probes (ESP) and Segment Limiter are installed at near the midpoint of the central cell ($z=0.33\text{m}$). Figure 2.15 shows the schematic drawing of the ESPs and Segment Limiter at the midpoint of the central cell ($z=0.33\text{m}$). The circuit models of ESP and Segment limiter are also indicated. These ESPs are biased to -200V and can measure the ion saturation current and fluctuations near the edge region. By using signals of two ESP, the direction of rotation of density fluctuation can be estimated [44].

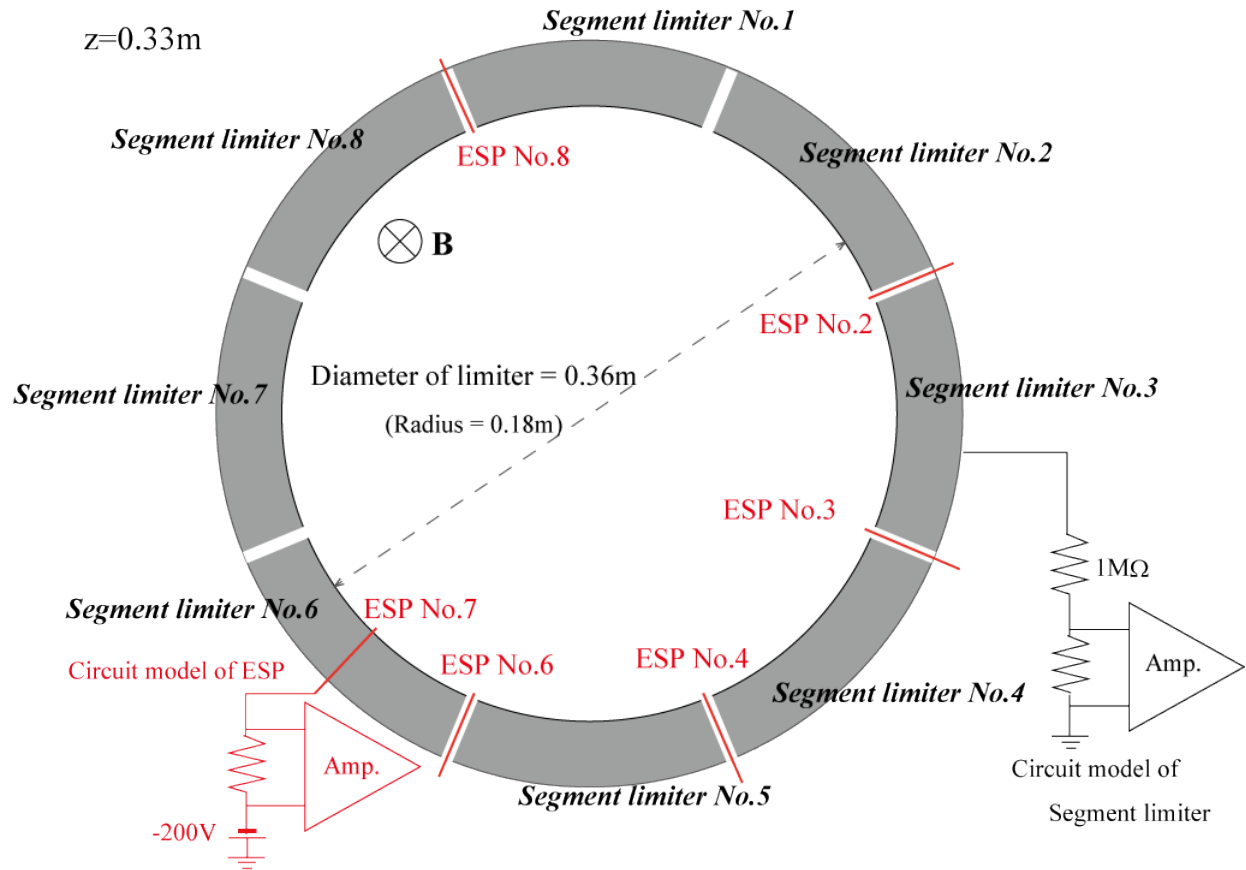


Figure 2.15 Schematic drawing of the Segment limiter and Electro Static Probes at the midpoint of the central cell ($z=0.33\text{m}$). The circuit models of Segment limiter and ESP are also indicated.

Chapter 3

Three dimensional full wave simulation

3.1 Three dimensional full wave simulation

TASK, which is developed by Prof. Atsushi Fukuyama in Kyoto University, is the one of the most developed integrated simulation code, and developing at the large scale experimental devices such as ITER and LHD [45]. The results by the integrated simulation code are very important to make of the experimental plan, the operation scenario, and so on [26]. TASK/WF is one of the major full wave simulation codes in the world, and the part of TASK code. This code solves Maxwell's equation in cold plasma with three dimensional finite elements methods (3D-FEM) including the effect of collision. By using 3D-FEM, the wave electric field including the complex magnetic field can be calculated.

3.1.1 Basic Equation

We calculate the dispersion relation in the static magnetic field. The direction of the static magnetic field is selected to z axis. The calculation begins from motion of charged particles in medium. In the isotropic medium, charged particles move to same direction of an electric field [46].

$$\delta \mathbf{u} = \mu \delta \mathbf{E} \quad (3.1)$$

where \mathbf{u} , μ , and \mathbf{E} denote velocity, mobility, and electric field, respectively. On the contrary, in the anisotropic medium, velocity of charged particles needs to be described with mobility tensor as

$$\delta \mathbf{u} = \vec{\mu} \cdot \delta \mathbf{E}. \quad (3.2)$$

So, current flowing in the medium is described with electric conductivity tensor, which is $\vec{\sigma} = n_0 q \vec{\mu}$.

$$\delta \mathbf{J} = \sum_s n_{s0} q_s \delta \vec{\mu}_s = \vec{\sigma} \cdot \mathbf{E} \quad (3.3)$$

where \mathbf{J} , s , n_{s0} , and q_s denote current, particle species, density for species, electric charge for species, respectively. Maxwell's equation of plane wave is written in Equation (3.4).

$$\mathbf{k} \times \mathbf{k} \times \delta \mathbf{E} + \frac{\omega^2}{c^2} \delta \mathbf{E} + i\omega\mu_0 \mathbf{J} = -i\omega\mu_0 \mathbf{J}_{\text{ext}} \quad (3.4)$$

where \mathbf{k} , ω , c , μ_0 and \mathbf{J}_{ext} denote wave vector, frequency, speed of light, magnetic permeability in vacuum and external current, respectively. The dielectric tensor is described as

$$\vec{\epsilon} \equiv \vec{I} + \frac{i}{\omega\mu_0} \vec{\sigma} = \vec{I} + i \sum_s \frac{n_{s0} q_s}{\omega\mu_0} \vec{\mu}_s. \quad (3.5)$$

Eq. (3.4) is rewritten with Eq. (3.5) as

$$\mathbf{k} \times \mathbf{k} \times \delta \mathbf{E} + \frac{\omega^2}{c^2} \vec{\epsilon} \cdot \delta \mathbf{E} = -i\omega\mu_0 \delta \mathbf{J}_{\text{ext}} \quad (3.6)$$

Wave vector is described as $\mathbf{k} = (k_x, 0, k_z)$, and Eq. (3.6) is written with substituting wave vector as

$$\mathbf{k} \times \mathbf{k} \times \delta \mathbf{E} \begin{pmatrix} -k_z^2 & 0 & k_x k_z \\ 0 & -k_x^2 - k_z^2 & 0 \\ k_x k_z & 0 & -k_x^2 \end{pmatrix} \cdot \delta \mathbf{E} \quad (3.7)$$

Eq. (3.7) is substituted into Eq. (3.4).

$$\vec{K} \cdot \delta \mathbf{E} = -i\omega\mu_0 \frac{\omega^2}{c^2} \delta \mathbf{J}_{\text{ext}} = -i \frac{1}{\omega \epsilon} \delta \mathbf{J}_{\text{ext}} \quad (3.8)$$

where \vec{K} denote dispersion tensor which defines in Eq. (3.9). In the

$$\vec{K} \equiv \begin{pmatrix} \epsilon_{xx} - N_z^2 & \epsilon_{xy} & \epsilon_{xz} + N_x N_z \\ \epsilon_{yx} & \epsilon_{yy} - N_x^2 - N_z^2 & \epsilon_{yz} \\ \epsilon_{zx} + N_x N_z & \epsilon_{zy} & \epsilon_{zz} - N_x^2 \end{pmatrix}, \quad (3.9)$$

refractive index is written by wave vector.

$$\mathbf{N} = \frac{\omega}{c} \mathbf{k} \quad (3.10)$$

Here, we consider the condition of propagation in medium without external current. Then,

$$\vec{K} \cdot \delta \mathbf{E} = 0 \quad (3.11)$$

is established. When electric field vector is not zero, refractive index vector needs to be zero as shown in

$$K \equiv |\vec{K}| = 0. \quad (3.12)$$

When Eq. (3.12) is satisfied, waves can propagate in medium.

In order to analyze plasma reaction, we need to solve the equation of motion. The fluid equation is given as following.

$$\begin{aligned} \frac{\partial n_s}{\partial t} + \frac{\partial}{\partial \mathbf{r}} \cdot (n_s \cdot \mathbf{u}_s) &= S_s \\ n_s m_s \left(\frac{\partial}{\partial t} \mathbf{u}_s + \mathbf{u}_s \frac{\partial}{\partial \mathbf{r}} \mathbf{u}_s \right) &= -\frac{\partial}{\partial \mathbf{r}} \cdot \vec{p}_s + n_s q_s (\mathbf{E} + \mathbf{u}_s \times \mathbf{B}) + R_s \\ \frac{d}{dt} (p n^{-\gamma}) &= 0 \end{aligned} \quad (3.13)$$

where \mathbf{r} , S_s , m_s , \mathbf{u}_s , \vec{p}_s , \mathbf{B} , R_s , and γ denote location of particle, time evolution of density, mass for species, velocity for species, pressure tensor, magnetic field strength, frictional force for species, and specific heat ratio, respectively. In Equation (3.13), we ignore effects of pressure and collision, because the temperature of plasmas is low enough and the frequency of waves is high enough. Equation (3.13) becomes

$$nm \left(\frac{\partial}{\partial t} \mathbf{u} + \mathbf{u} \frac{\partial}{\partial \mathbf{r}} \mathbf{u} \right) = nq(\mathbf{E} + \mathbf{u} \times \mathbf{B}) - nm\nu \mathbf{u} \quad (3.14)$$

where ν denotes collision frequency. We assume that the wave amplitude is small enough. The perturbation of velocity, electric field strength, and magnetic field strength is introduced as

$$\begin{aligned} \mathbf{u} &= \delta \mathbf{u} \exp(i\mathbf{k} \cdot \mathbf{r} - i\omega t) \\ \mathbf{E} &= \delta \mathbf{E} \exp(i\mathbf{k} \cdot \mathbf{r} - i\omega t) \end{aligned} \quad (3.15)$$

$$\mathbf{B} = \mathbf{B}_0 + \delta\mathbf{B}\exp(i\mathbf{k} \cdot \mathbf{r} - i\omega t).$$

We rewrite Equation (3.14) in liner form with substituting Equation (3.15) as

$$-i\omega\delta\mathbf{u} = \frac{q}{m}(\delta\mathbf{E} + \delta\mathbf{u} \times \delta\mathbf{B}_0) - \nu\delta\mathbf{u}. \quad (3.16)$$

We rewrite Eq. (3.16) in ingredient form as

$$-i\omega \begin{pmatrix} \delta u_x \\ \delta u_y \\ \delta u_z \end{pmatrix} = \frac{q}{m} \begin{pmatrix} \delta E_x \\ \delta E_y \\ \delta E_z \end{pmatrix} + \frac{qB_0}{m} \begin{pmatrix} \delta u_y \\ -\delta u_x \\ 0 \end{pmatrix} - \nu \begin{pmatrix} \delta u_x \\ \delta u_y \\ \delta u_z \end{pmatrix}. \quad (3.17)$$

In Eq. (3.17), terms including $\delta\mathbf{u}$ are transported to left side as

$$\begin{pmatrix} -i\omega + \nu & -\omega_c & 0 \\ \omega_c & -i\omega + \nu & 0 \\ 0 & 0 & -i\omega + \nu \end{pmatrix} \cdot \begin{pmatrix} \delta u_x \\ \delta u_y \\ \delta u_z \end{pmatrix} = \frac{q}{m} \begin{pmatrix} \delta E_x \\ \delta E_y \\ \delta E_z \end{pmatrix}. \quad (3.18)$$

We solve Eq. (3.18) about $\delta\mathbf{u}$ as

$$\delta\mathbf{u} = \frac{iq}{m\omega} \begin{pmatrix} \frac{(\omega+iv)^2}{(\omega+iv)^2-\omega_c^2} & \frac{i(\omega+iv)\omega_c}{(\omega+iv)^2-\omega_c^2} & 0 \\ \frac{-i(\omega+iv)\omega_c}{(\omega+iv)^2-\omega_c^2} & \frac{(\omega+iv)^2}{(\omega+iv)^2-\omega_c^2} & 0 \\ 0 & 0 & 1 \end{pmatrix} \cdot \delta\mathbf{E}. \quad (3.19)$$

In Eq. (3.19), tensor of the right term is the mobility tensor. We calculate dielectric tensor with substituting into Eq. (3.5). The dielectric tensor is shown as

$$\vec{\epsilon} = \vec{I} + \sum_s \frac{in_s q_s}{\omega \epsilon_0} \vec{\mu}_s = \begin{pmatrix} S & -iD & 0 \\ iD & S & 0 \\ 0 & 0 & P \end{pmatrix} \quad (3.20)$$

$$S = 1 - \sum_s \frac{(\omega + iv)^2}{\omega} \cdot \frac{\omega_{ps}^2}{(\omega + iv)^2 - \omega_{cs}^2}$$

$$D = \sum_s \frac{\omega_{cs} \omega_{ps}^2}{\omega((\omega + iv)^2 - \omega_{cs}^2)} \quad (3.21)$$

$$P = 1 - \sum_s \frac{\omega_{ps}^2}{\omega(\omega + iv)^2}$$

where $\vec{\epsilon}$, \vec{I} , and $\vec{\mu}_s$ denote the dielectric tensor, the unit tensor, and the mobility tensor, respectively. S, D, and P denote as Eq. (3.21).

In the TASK/WF,

$$\nabla \times \nabla \times \mathbf{E} - \frac{\omega^2}{c^2} \vec{\epsilon} \cdot \mathbf{E} = i\omega\mu_0 \mathbf{J}_{ext} \quad (3.22)$$

is solved by 3D-FEM. In Eq. (3.22), \mathbf{E} , ω , c , $\vec{\epsilon}$, μ_0 , and \mathbf{J}_{ext} denote the electric field, frequency, speed of light, the dielectric tensor, permeability, and the external antenna current, respectively. In this calculation, it is assumed that there is the cold plasma including collision effects taken in the dielectric tensor.

$$\omega' \equiv \omega + i\nu$$

$$\omega_{cs} = \frac{Zq_s B_0}{m_s} \quad (3.23)$$

$$\omega_{ps} = \sqrt{\frac{n_s q_s^2}{m_s \epsilon_0}}$$

where ω' is defined as shown in Eq. (3.23). ω_{cs} and ω_{ps} denote the cyclotron frequency and the plasma frequency for species, respectively. In Eq. (3.23), ν , Z , q_s , B_0 , m_s , n_s , and ϵ_0 denote collision frequency, atomic value, electric charge for species, magnetic field strength, mass for species, density for species, and permittivity in vacuum, respectively.

In the TASK/WF, the effect of the cyclotron damping is written by the collision frequency. In the dielectric tensor as shown in Eqs. (3.20) and (3.21), there are the matrix elements becoming the purely imaginary number on the resonance layer. Here, we calculate the radiated power and the absorbed power based on

$$P = \text{Re}\{J \cdot \mathbf{E}^*\} \quad (3.24)$$

where J , and \mathbf{E}^* are the current and the conjugate wave electric field strength. In the case of the radiated power, the external current flowing on antenna is substituted in Eq. (3.24). The radiated power is calculated by integrating along to elements which are flowed the antenna current, and shown as

$$P = \int J_{ext} \cdot \mathbf{E}^* dV. \quad (3.25)$$

The absorbed power of each elements is calculated by using the induced current by the waves. The induced current is shown in Eq. (3.3). The absorbed power of elements is shown as

$$\begin{aligned} P_{abs} &= \frac{1}{2} \mathbf{J} \cdot \mathbf{E}^* \\ &= \frac{1}{2} \mathbf{E}^* \cdot \vec{\sigma}_s^H \cdot \mathbf{E} \end{aligned} \quad (3.26)$$

where $\vec{\sigma}_s^H$ denotes the electric conductivity tensor for species. The wave magnetic field is calculated by Faraday's law as

$$\begin{aligned} B_r &= -i \frac{c}{\omega} \frac{1}{r} \left[\frac{\partial}{\partial z} (r E_\theta - i m E_z) \right] \\ B_\theta &= -i \frac{c}{\omega} \left[\frac{\partial}{\partial r} E_z - \frac{\partial}{\partial z} E_r \right] \\ B_z &= -i \frac{c}{\omega} \frac{1}{r} \left[i m E_r - \frac{\partial}{\partial r} (r E_\theta) \right]. \end{aligned} \quad (3.27)$$

3.1.2 Boundary condition

In TASK/WF, the elements are surrounded by the conducting wall. On the conducting wall, the tangential electric field is zero. In case of calculation between the central cell and the anchor cell, the collision frequency is selected to be high for preventing reflection of waves at the boundary in the end of the z-direction.

3.1.3 Introduction of Multi-Processing Code

In order to calculate more effectively, the multi-processing code is introduced for phase-control experiments on GAMMA 10. In this code, MULTifrontal Massively Parallel sparse direct Solver (MUMPS) is used for the solver. By using MUMPS, parallel processing by using a multi-core processor is enabled. Figure 3.1 shows the number of processor dependence of calculation time with the test file for GAMMA 10. The decrease of calculation time with the increase number of processor is observed. In the multi-processing code, we can calculate the test code, which is needed longer than 20 hours in the old code, shorter than 6 hours with twelve processors by using macro3F in Plasma Research Center at University of Tsukuba. The macro3F has two 6-core Intel Xeon processors (2.93GHz) and 64GB memories.

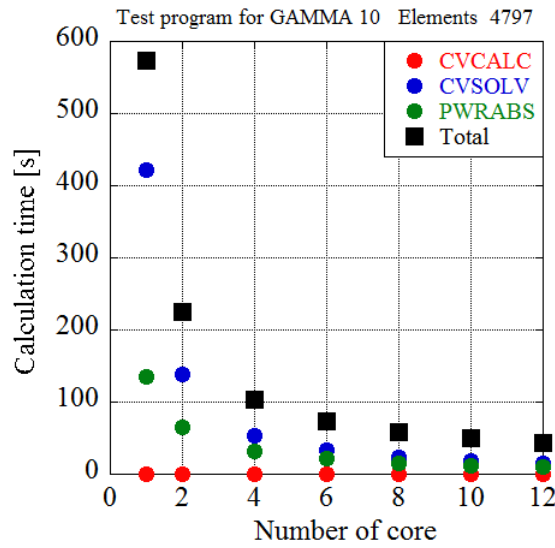


Figure 3.1 Number of processors dependence of the calculation time with test program for GAMMA 10. The decrease of the calculation time is observed.

3.4 Setup for Wave Analysis of GAMMA 10 experiments

3.4.1 Elements for Phase-control Experiments

In order to calculate wave propagation in the phase-control experiments, elements are constructed between the central cell and the west anchor cell on GAMMA 10, in which length is 10.9m ($-3.3 \leq z \leq 7.6$). Figure 3.2 shows the schematic drawing of elements on z-y plane, the location of ICRF antennas, and the shape of ICRF antennas in TASK/WF. The element length in radial direction is selected 0.03m at the core plasma region ($x, y=0 \sim 0.24$ m), and selected to 0.1m at the peripheral region ($x, y=0.24 \sim 0.5$ m). The element length in axial direction is selected 0.03m in the central cell ($-3.3 \leq z \leq 2.8$), and selected 0.01m in the anchor cell ($2.8 \leq z \leq 7.6$) in order to calculate wave propagation in detail.

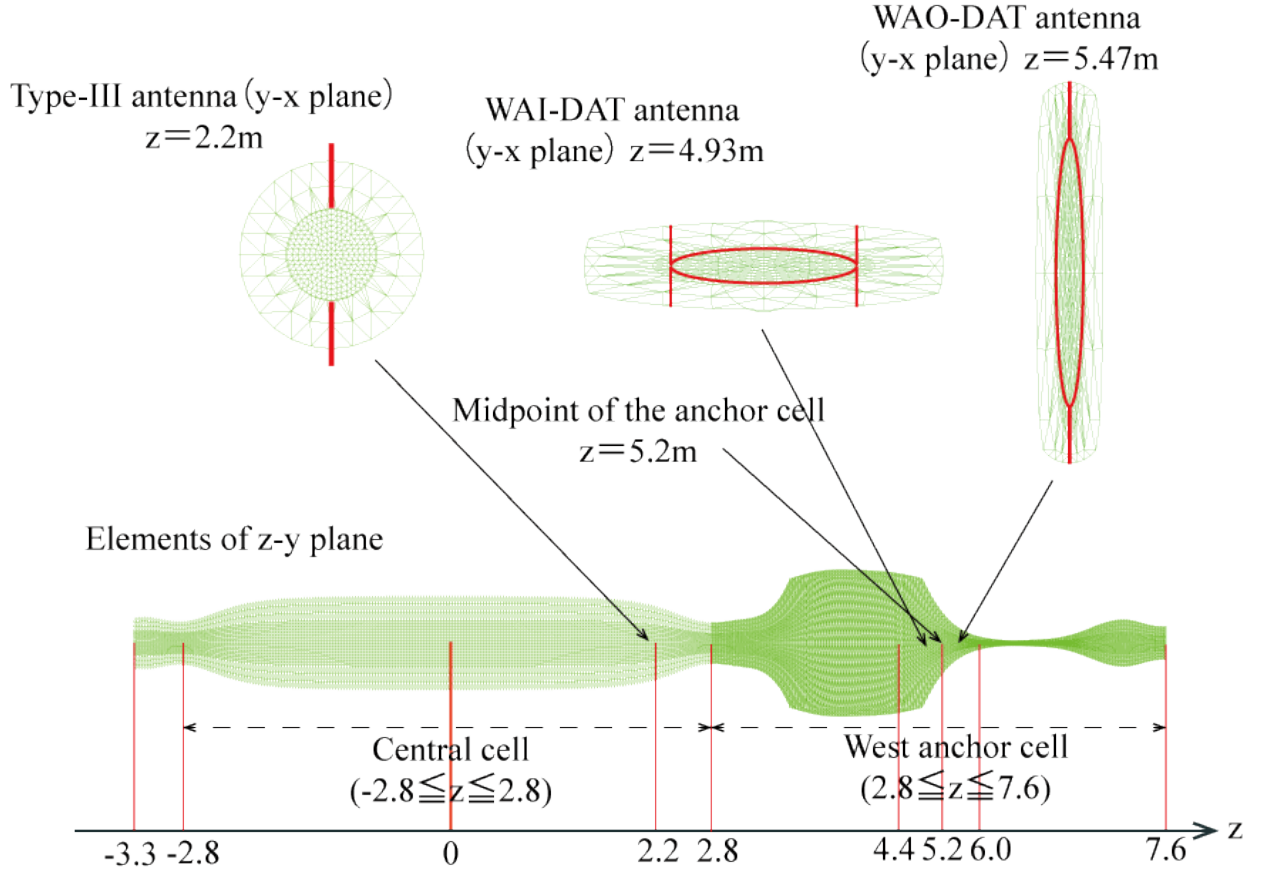


Figure 3.2 Schematic drawing of elements on z-y plane, the location of ICRF antennas, and the shape of ICRF antennas in wave analysis.

3.4.2 Profiles of Parameters for Wave Analysis

3.4.2.1 Magnetic Field Strength

The magnetic field strength is determined from experimental setting up. The magnetic field strength is 0.41T at the midplane of the central cell, and 0.6T at the midpoint of the anchor cell. Figure 4.3 shows the profile of magnetic field strength on (a) z-x plane, (b) z-y plane, and (c) z axis between the central cell and the west anchor cell ($-3.3 \leq z \leq 7.6$) in TASK/WF. The red lines, which are magnetic field lines of the $R_{cc}=0.18m$, indicate the plasma region. It is clear that the closed magnetic field strength layer exists in the anchor cell.

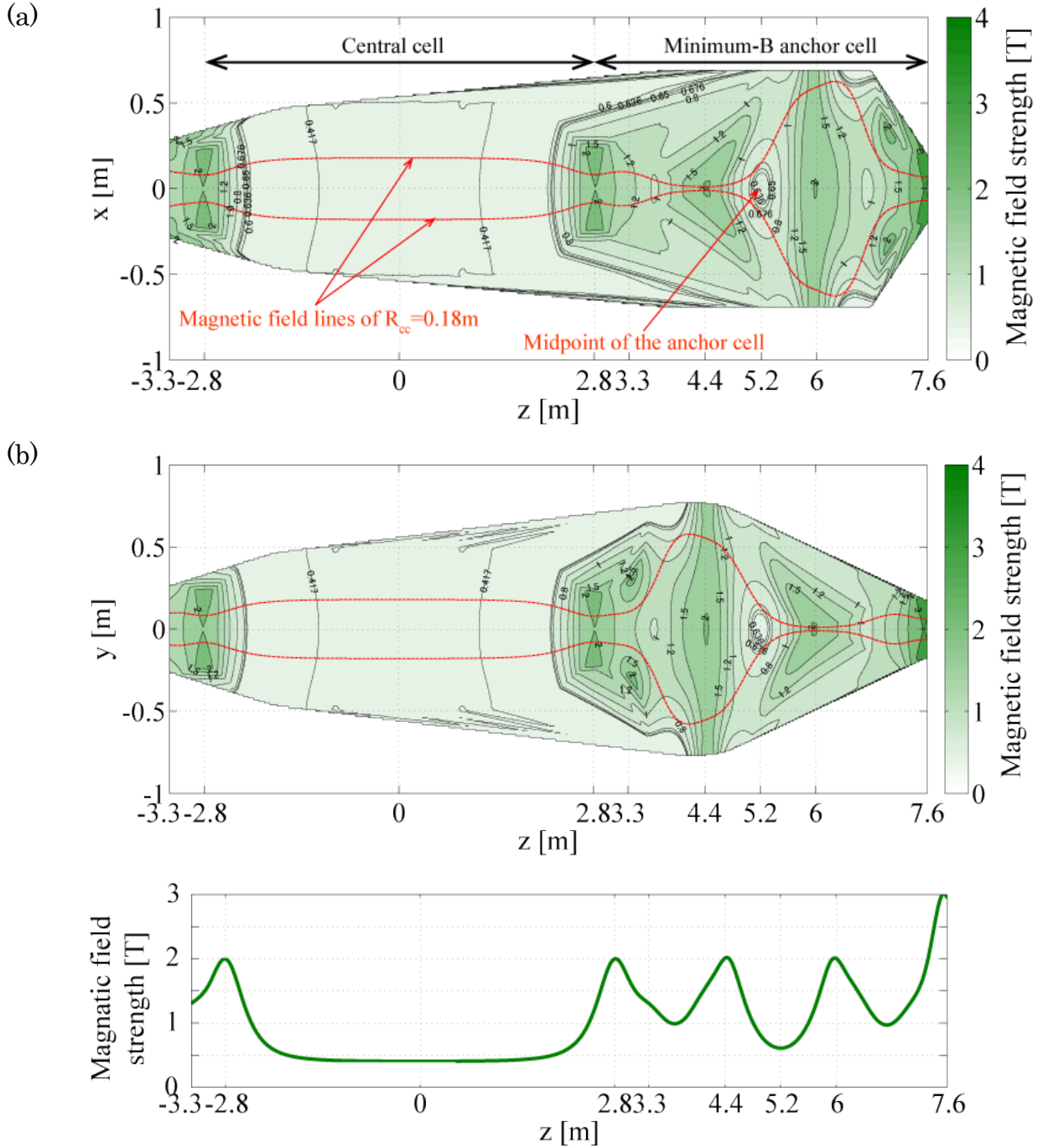


Figure 3.3 Profile of magnetic field strength on (a) z-x plane, (b) z-y plane, and (c) z axis between the central cell and the west anchor cell ($-3.3 \leq z \leq 7.6$) in TASK/WF

3.4.2.2 Electron Density

The profile of density is determined from results of experiments. Figure 3.4 shows the profile of density on (a) z-x plane, (b) z-y plane, and (c) z axis between the central cell and the west anchor cell ($-3.3 \leq z \leq 7.6$) in TASK/WF, when the top of core density is $2.0 \times 10^{18} \text{ m}^{-3}$.

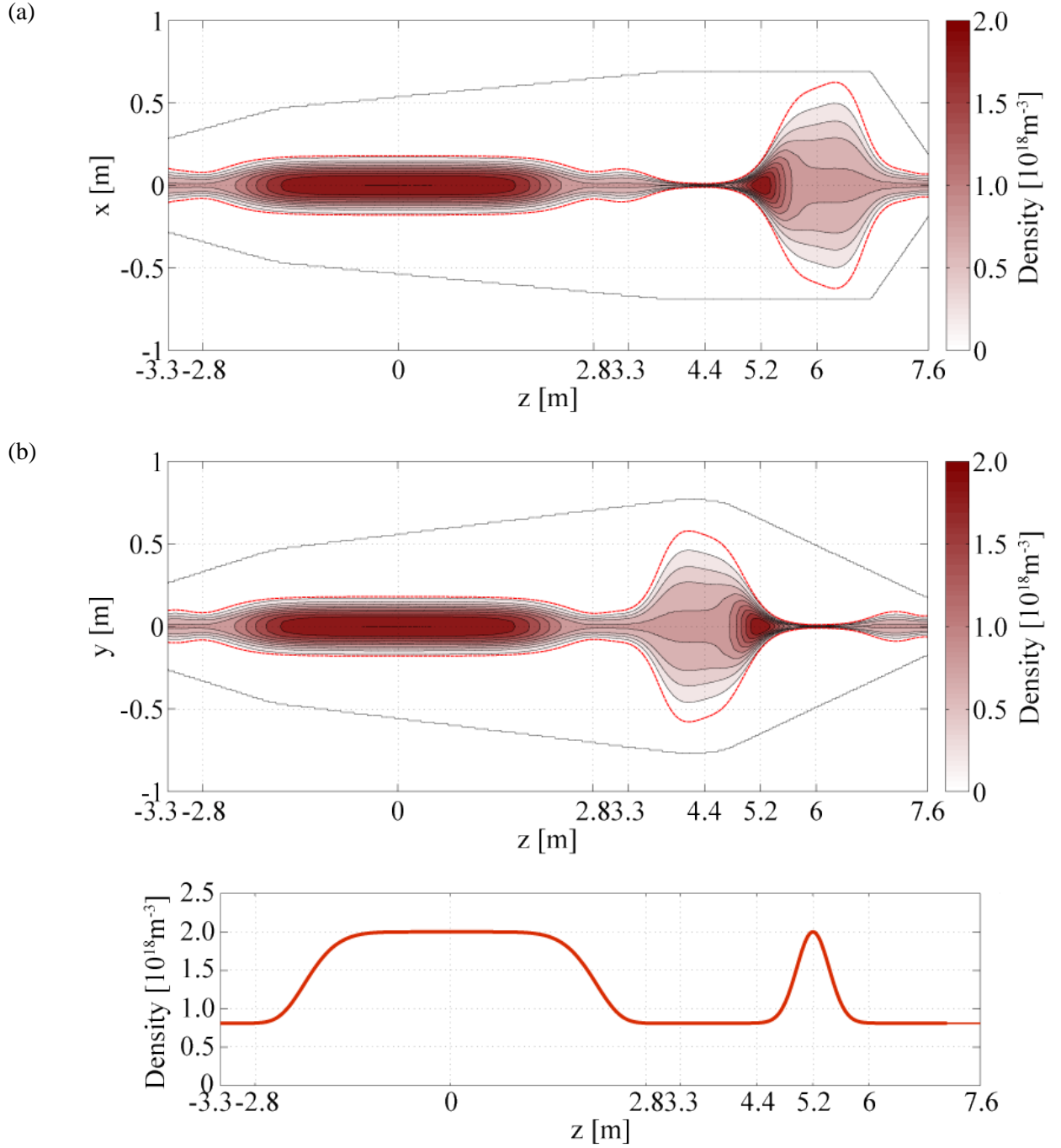


Figure 3.4 The profile of density on (a) z - x plane, and (b) z - y plane, (c) z axis between the central cell and the west anchor cell in TASK/WF

The profile of density in radial direction in TASK/WF is determined from results of experiments. Figure 3.5 shows the typical time evolution of (a) ICRF power and (b) line-integrate density at the central cell ($z=-0.6$ m), the throat ($z=-2.8$ m), and the east anchor cell ($z=5.2$ m) of the phase control experiments with Type-III (East) and EAI-DAT antennas. RF power from EAI-DAT antenna with 9.9MHz is inputted from 200 to 240ms. The increasing of line-integrated density during inputting RF power is observed. The

line-integrated density at the central cell is $\sim 5 \times 10^{13} \text{cm}^{-2}$ without RF3, and $\sim 6 \times 10^{13} \text{cm}^{-2}$ with RF3. The radial profile of electron density at the central cell ($z=-0.6\text{m}$) is measured by microwave reflectmeter. Figure 3.6 shows (a) the radial profile of electron density measured in phase-control experiments, and (b) the radial profile of the normalized density. From Fig. 4.6(a), electron density at the midpoint of the central cell is indicated near $2.0 \times 10^{18} \text{m}^{-3}$ at 120, 150 and 200ms, and $\sim 3.0 \times 10^{18} \text{m}^{-3}$ at 220ms. In order to investigate the shape of the radial profile, profiles are standardized by the electron density at the midpoint. According to the Fig. 3.6(b), it is observed that changes of radial profile is small. The radial profile of the density in TASK/WF is decided as green lines indicating in Fig 4.6(b).

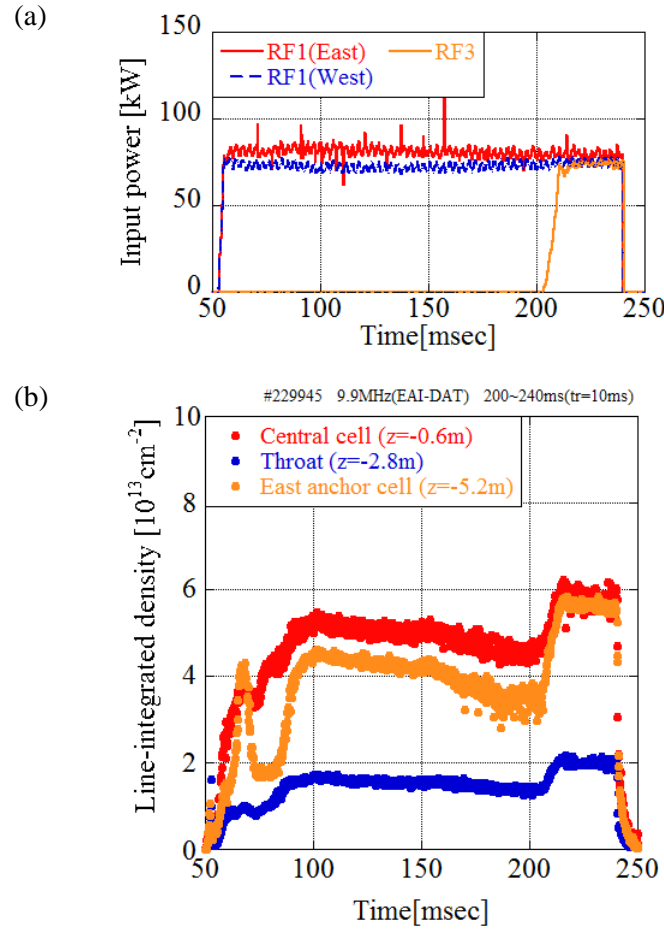


Figure 3.5 Time dependence of ICRF power and (b) Line-integrate density at the central cell($z=-0.6\text{m}$), the throat ($z=-2.8\text{m}$), and the east anchor cell($z=-5.2\text{m}$).

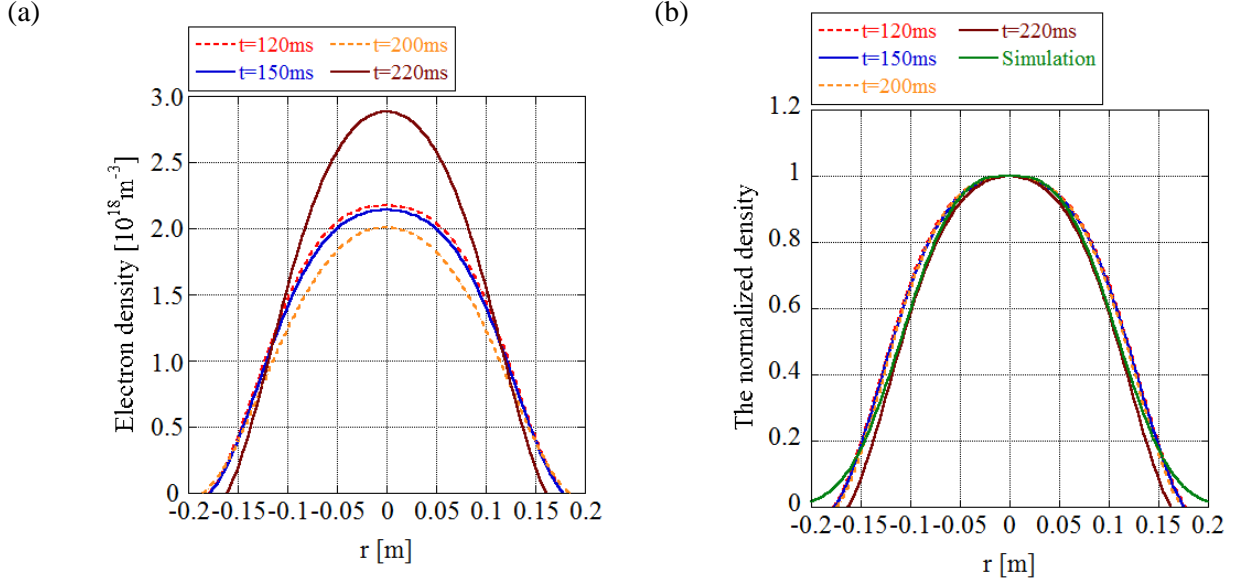


Figure 3.6 (a)Radial profile of electron density measured in phase-control experiments, and (b)radial profile of the normalized density

3.4.2.3 Antenna current

In the experiments, Type-III in the central cell, WAI-DAT, and WAO-DAT antennas in the anchor cell are used for excitation of ICRF waves. Figure 3.7 shows the schematic drawing of (a)Type-III, (b)WAI-DAT, and (c)WAO-DAT antennas. The direction of antenna current is also indicated. Antennas strongly couple to the waves which have the structure of $m=\pm 1$ in the azimuthal direction because of their antenna current.

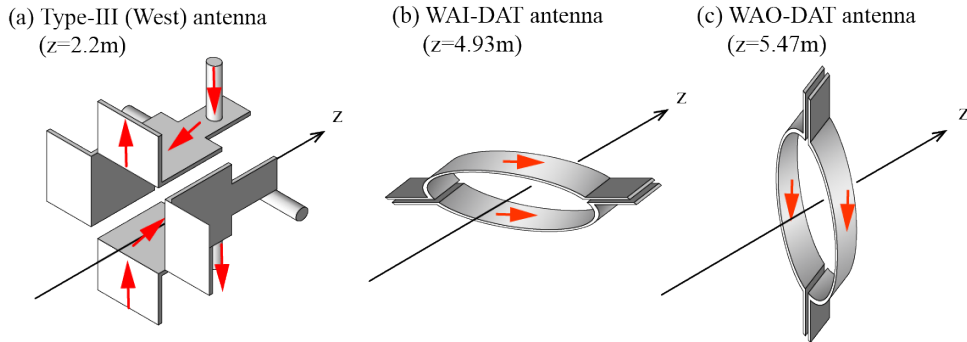


Figure 3.7 Schematic drawing of (a)Type-III, (b)WAI-DAT, and (c)WAO-DAT antenna. The direction of antenna current is also indicated.

Chapter 4

Experimental Observation of Antenna Modification

4.1 Antenna Loading of Anchor ICRF Antenna

In the standard discharge, the ion-heating in the anchor cell is performed by ICRF waves excited by Type-III antennas at the both ends of the central cell with mode-conversion of fast wave to slow wave. In order to heat ions efficiently in the anchor cell independently, the direct ion-heating in the anchor cell had been introduced by using straight Bar-type antenna in the anchor cell and performed stabilization effect of the whole plasma had been confirmed [47]. However it had been observed that the antenna loading of Bar-type is small. In order to improve antenna loading, the shape dependence of antenna loading resistance was calculated by TASK/WF. In the calculation, the antenna loading resistance is calculated in cases of three types of antennas; one is the Bar-type which is straight shape. The other is a half elliptical shape antenna which is so-called Single Arc Type (SAT) antenna. The other is a elliptical shape antenna surrounding magnetic flux tubes, which is so-called and Double Arc Type (DAT) antenna. Figure 4.1 shows the schematic drawing of the elements and antennas in the numerical simulation. (a)Bar-type antenna, (b)SAT antenna, and (c)DAT antenna are indicated. Figure 4.2 shows the frequency and density dependence of the antenna loading resistance of Bar-type antenna, SAT antenna, and DAT antenna. In this calculation, the plasma parameters are determined as following; core density is 1.0, 2.0, $5.0 \times 10^{18} \text{m}^{-3}$, and peripheral density is $1.0 \times 10^{17} \text{m}^{-3}$. The antenna location is $z=5.475\text{m}$, which is 0.275m from the midpoint of the anchor cell. The closed resonance layer of 9.3~10.5MHz ICRF waves exists in the plasma region. By the closed resonance layer and the profile of density, the peak values are indicated near 10MHz. According to this calculation, it is clearly observed that the antenna loading resistance increases from Bar-type antenna to SAT antenna, and from SAT antenna to DAT antenna. In case of change antenna from Bar-type antenna to SAT antenna, the increase of antenna loading resistance is observed by fitting the shape of the plasma cross section at the location of the anchor antenna. In case of antenna change from SAT antenna to DAT antenna, the increase of antenna loading may be caused by fitting antenna with plasma shape. The fragment of DAT antenna is twice large than that of SAT antenna. It is observed that the increase antenna loading resistance is performed by changing antenna shape from Bar-type antenna to DAT antenna. The density dependence of antenna loading resistance is small [35].

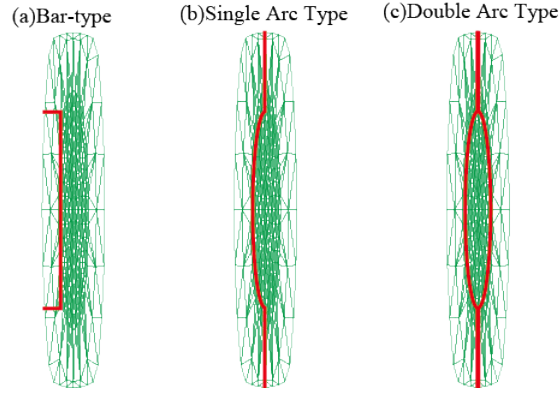


Figure 4.1 Schematic drawing of the elements at the location of antennas, (a)Bar-type antenna, (b)Single Arc Type antenna, and(c)Double Arc Type antenna in the numerical simulation

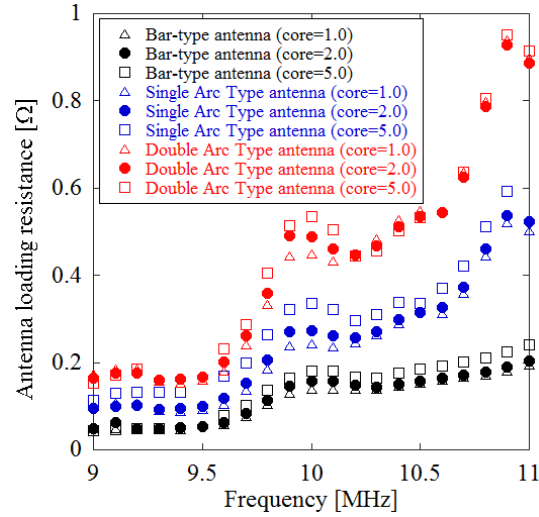


Figure 4.2 The frequency and density dependence of the antenna loading resistance of Bar-type antenna, Single Arc Type antenna, and Double Arc Type antenna by TASK/WF

In order to investigate improvement of antenna loading in the experiments, the antenna loading and SED signal are measured in cases of Bar-type and DAT antennas. Figure 4.3 shows the power dependence of (a) the antenna loading, and (b) the normalized SED signal in the anchor cell. In these experiments, 9.7MHz ICRF waves are excited by Bar-type or DAT antennas. The anchor antenna exists in the east and west anchor cell. From Fig. 4.3 (a), the antenna loading of the Bar-type antenna is less than ~ 0.2 , and the that of the DAT antenna is more than 0.5. It is clearly observed that the more than three times increase of antenna loading. The decrease of the antenna loading at the large input power appears. It is considered as the one reason that the high voltage is applied on the anchor antenna, so plasma near the antenna is repelled. According to Fig. 4.3 (b), the more increase of SED signal is observed in the direct anchor heating experiments with 9.7MHz waves. 9.7MHz waves are only excited by the anchor antenna, so it is considered that the increase of SED signal is caused by the 9.7MHz waves from the anchor antennas. By changing the anchor antenna from Bar-type antenna to DAT antenna, the more effective ion-heating in the anchor cell is achieved. [36].

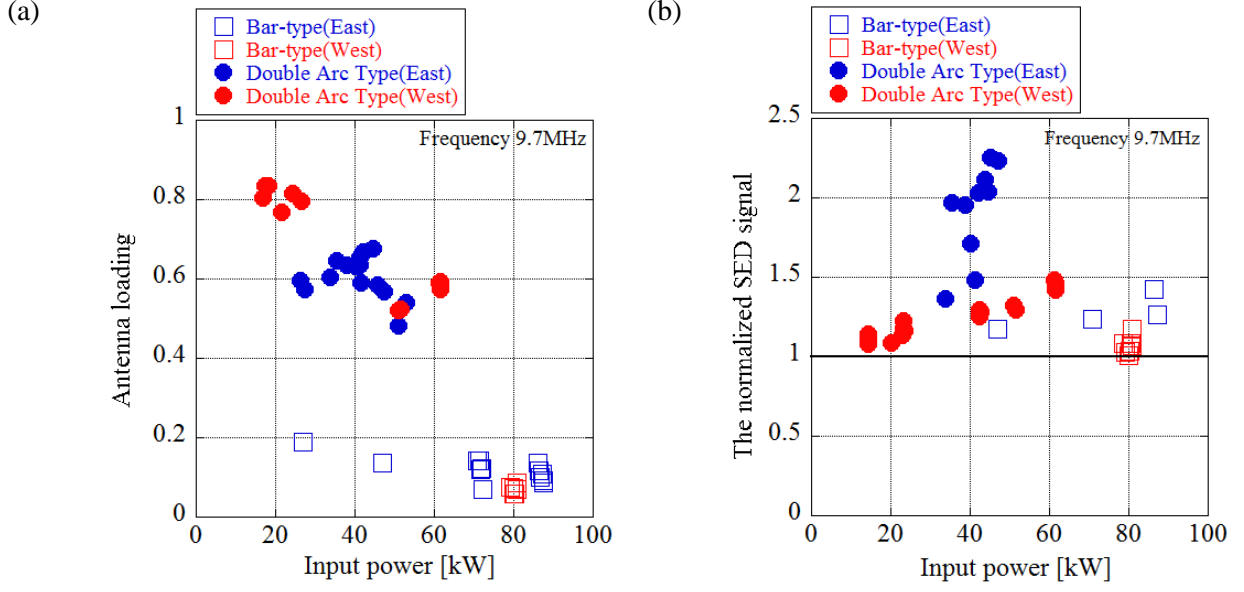


Figure 4.3 The power dependence of (a) the antenna loading of the anchor antenna, and (b) the normalized SED signal in the anchor cell. The 9.7MHz ICRF waves are used for these anchor heating experiments.

4.2.2 Frequency Dependence of Anchor Heating

In order to investigate most suitable frequency for enhancement of ion-heating in the anchor cell with ICRF antennas in the anchor cell, the frequency dependence is observed in the experiments. In these experiments, 8.0, 9.7, and 10.3MHz waves are excited by WAO-DAT antenna, which is installed at $z=5.475\text{m}$. Figure 4.4 shows (a) the schematic drawing of magnetic field lines, (b) the magnetic field strength, and (c) the value of ω/Ω_{ci} of 8.0, 9.7, and 10.3MHz waves from the central cell to the west anchor cell. 8.0MHz waves have the resonance layer only at the end of the central cell. 9.7MHz waves have the resonance layer at the anchor cell and the end of the central cell as shown in Fig. 4.4(c). 10.3MHz waves have the resonance layer at same as 9.7MHz waves, in addition to this, wave interference occurs because 10.3MHz waves are also excited by Type-III antennas for the ion-heating in the anchor cell. Figure 4.5 shows the input power dependence of (a) the normalized SED signal and (b) the line-integrated density in the central cell using 8.0, 9.7, 10.3MHz waves excited by WAO-DAT antenna. In case of exciting 10.3MHz waves, there are two conditions. The orange markers indicates the power dependence, on the other hand, the black squares indicates the phase dependence of which conditions are shown in following chapter, respectively. On the contrary, there is no resonance layer of 8.0MHz waves in the anchor cell. From Fig. 4.4, it is clearly observed that the enhancement of ion-heating in the anchor cell is performed in the case of exciting 9.7MHz or 10.3MHz waves, and the increase of line-integrated density in the central cell is performed in case of 9.7MHz waves and 10.3MHz waves with phase-control. In the case of 8.0MHz waves and 10.3MHz waves with phase-control, there are conditions that plasmas cannot be kept with increase

power. In the case of 8.0MHz waves, magnetic field lines at the ends of the central cell has bad curvature as shown in Fig. 4.4(a). 8.0MHz waves propagate to the end of the central cell without absorption, because there are no resonance layers of 8.0MHz waves in the anchor cell. In the case of 10.3MHz waves with phase-control, there may be conditions which are decreasing ion-heating in the anchor cell by results of wave influence.

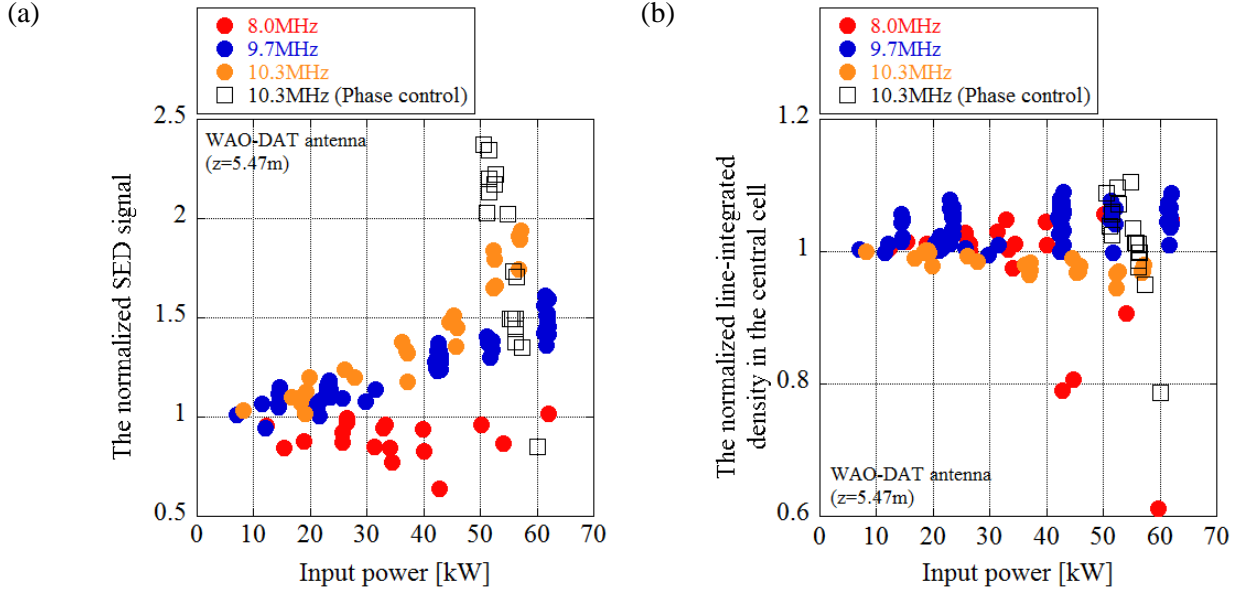


Figure 4.4 Power dependence of (a) the normalized SED signal and (b) the line-integrated density in the central cell using 8.0, 9.7, 10.3MHz waves excited by WAO-DAT antenna.

Here, we consider the conditions that plasmas cannot be kept with increase power in cases of using 8.0MHz waves and 10.3MHz with phase control. It is considered as a one of the reason about plasmas cannot be kept with increase power in cases of using 8.0MHz waves that MHD stability decreases by heating at the end of the central cell because there are bad curvature magnetic field strength at the resonance layer of 8.0MHz waves. Because the resonance layer of 8.0MHz don't exist in the anchor cell, 8.0MHz waves propagates to the end of the central cell without absorbing in the anchor cell. In order to investigate propagating 8.0MHz waves, the absorbed power of ICRF waves at the end of the central cell is calculated by TASK/WF. Figure 4.5 shows the frequency dependence of the normalized absorbed power at the end of the central cell in the cases of WAO-DAT and WAI-DAT antenna. In this calculation, waves are excited by WAO-DAT or WAI-DAT antenna in the anchor cell with same input power, and the core density of the central cell is determined as $2.0 \times 10^{18} \text{m}^{-3}$. The resonance layers of 8.0, 9.7, 10.3MHz exist at the end of the central cell. It is clearly observed that 8.0MHz and 9.0MHz waves, which have no resonance layer in the anchor cell, heats more strongly than waves which have resonance layer in the anchor cell. Figure 4.6 shows the time evolution of FFT amplitude of ESP ch4 installed at the central cell (a) in the case of input power of $\sim 15\text{kW}$, and (b) input power of $\sim 70\text{kW}$, (c) Power spectrum of FFT of ESPs and (d) phase-dependence of two ESPs of which phase difference is 45-degree when 8.0MHz waves are excited by WAO-DAT antenna are shown. ESPs are installed in the central cell as shown in Fig. 2.15. From Fig 4.6(a) and (b), it is observed that the instability of $\sim 4\text{kHz}$ appears during 8.0MHz waves. The rotation direction of this instability is measured by

ESP ch3 and ch4. From Fig. 4.6(c) and (d), the phase difference of this instability is observed as near 60-degree. The difference between ESP ch3 and ch4 is 45-degree. It is calculated that this density fluctuation has left-hand rotation, and mode -1 and -2. By these results, this instability is considered to be a flute type instability. According to these results in the numerical simulation and the experiments, it is clearly observed that the decrease of the MHD stability is one of the reason.

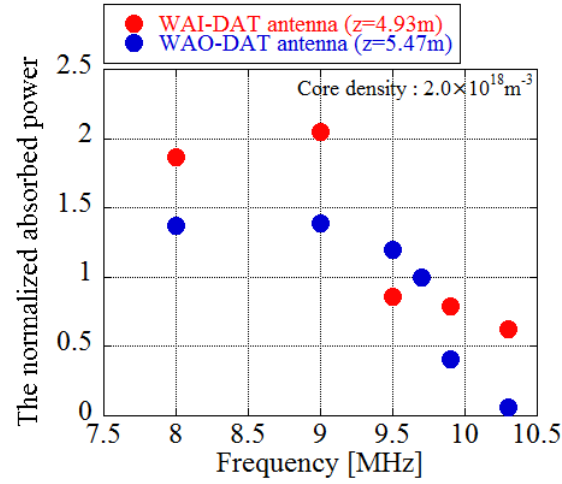


Figure 4.5 Frequency dependence of the normalized absorbed power at the end of the central cell ($1.9 < z < 2.3$) in the cases of WAO-DAT antenna, and WAI-DAT antenna.

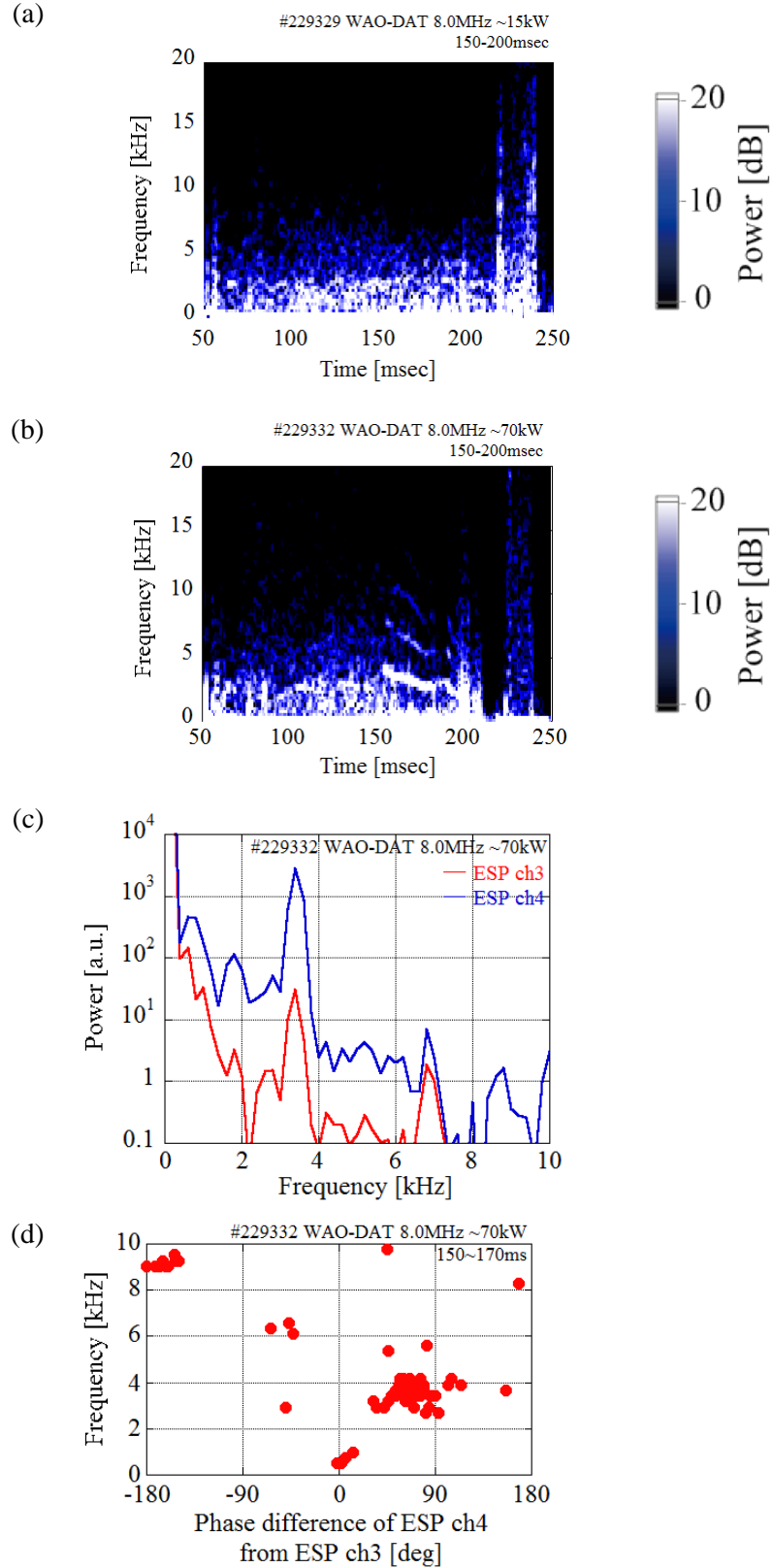


Figure 4.6 Time evolution of FFT amplitude of ESP ch4 installed at the central cell (a) in case of inputting power of $\sim 15\text{kW}$, and (b) inputting power of $\sim 70\text{kW}$. The frequency dependence of (c) FFT amplitude of ESP ch4 and (d) phase-dependence of ESP ch4 from ESP ch3 when 8.0MHz waves are excited by WAO-DAT antenna.

Chapter 5

Effective Heating with Phase-Control Experiments

According to Chapter 4, it is clearly observed that the more enhancement of ion-heating in the anchor cell is performed by phase-control experiments between two antennas. In order to perform enhancement of ion-heating in the anchor cell, the propagation and absorption of ICRF waves in phase-control experiments on GAMMA 10 are analyzed in this chapter.

5.1 Concept of phase-control experiments

In order to control the wave propagation, phase-control experiments between RF waves from two antennas are performed [24]. Figure 5.1 shows the schematic drawing of phase control experiments in a simple model. In the model on cylindrical plasma, two antennas exist along the magnetic field. The direction of wave propagation is evaluated from Equation 5.1, 5.2 and 5.3. In these equations, P_0 , P_L , P_C , P_R , δ , k_z , and d , denote input power from antennas, power at left side of both antennas, power between both antennas, power to the right side of both antennas, phase difference of antenna current, wave number, and distance between both antennas, respectively. It is clearly observed that the direction of wave propagation can be control by phase difference of antenna current, wave number, and distance between both antennas.

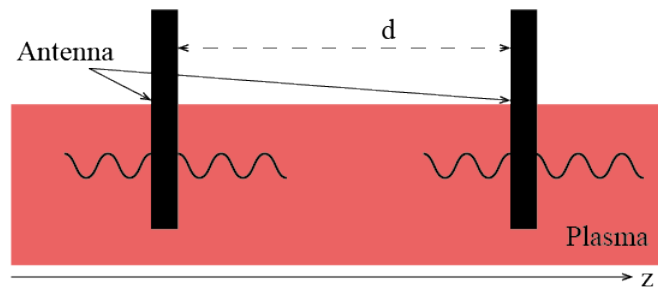


Figure 5.1 Schematic drawing of phase-control experiments in simple model

$$P_L/P_0 = 1 + \cos (\delta - k_z d) \quad (5.1)$$

$$P_C/P_0 = 1 + \cos \{\delta + k_z (2z - d)\} \quad (5.2)$$

$$P_R/P_0 = 1 + \cos (\delta + k_z d) \quad (5.3)$$

5.2 Phase-control experiments on GAMMA 10

On GAMMA 10, phase-control experiments are introduced by using Type-III, EAI-DAT, WAI-DAT, and WAO-DAT antennas, and have three conditions [48, 49]. Figure 5.2 shows the schematic drawing of phase-control experiments in case of (a) Type-III (East) and EAI-DAT antennas with 9.9MHz waves in the east side, and (b) Type-III (West) and WAI-DAT or WAO-DAT antennas with 10.3MHz waves in the west side. There are two types of relationship about location of antennas and the resonance layer in the anchor cell. In cases of (a) Type-III (East) and EAI-DAT antennas with 9.9MHz waves in the east side, and (b) Type-III (West) and WAI-DAT antennas with 10.3MHz waves, the resonance layer in the anchor cell is located outside of both antennas. The distance of two antennas is 2.7m in length. On the contrary, in case of the Type-III (West) and WAO-DAT antennas with 10.3MHz waves in the west side, the resonance layer in the anchor cell is located between both antennas. The distance of two antennas is 3.3m in length.

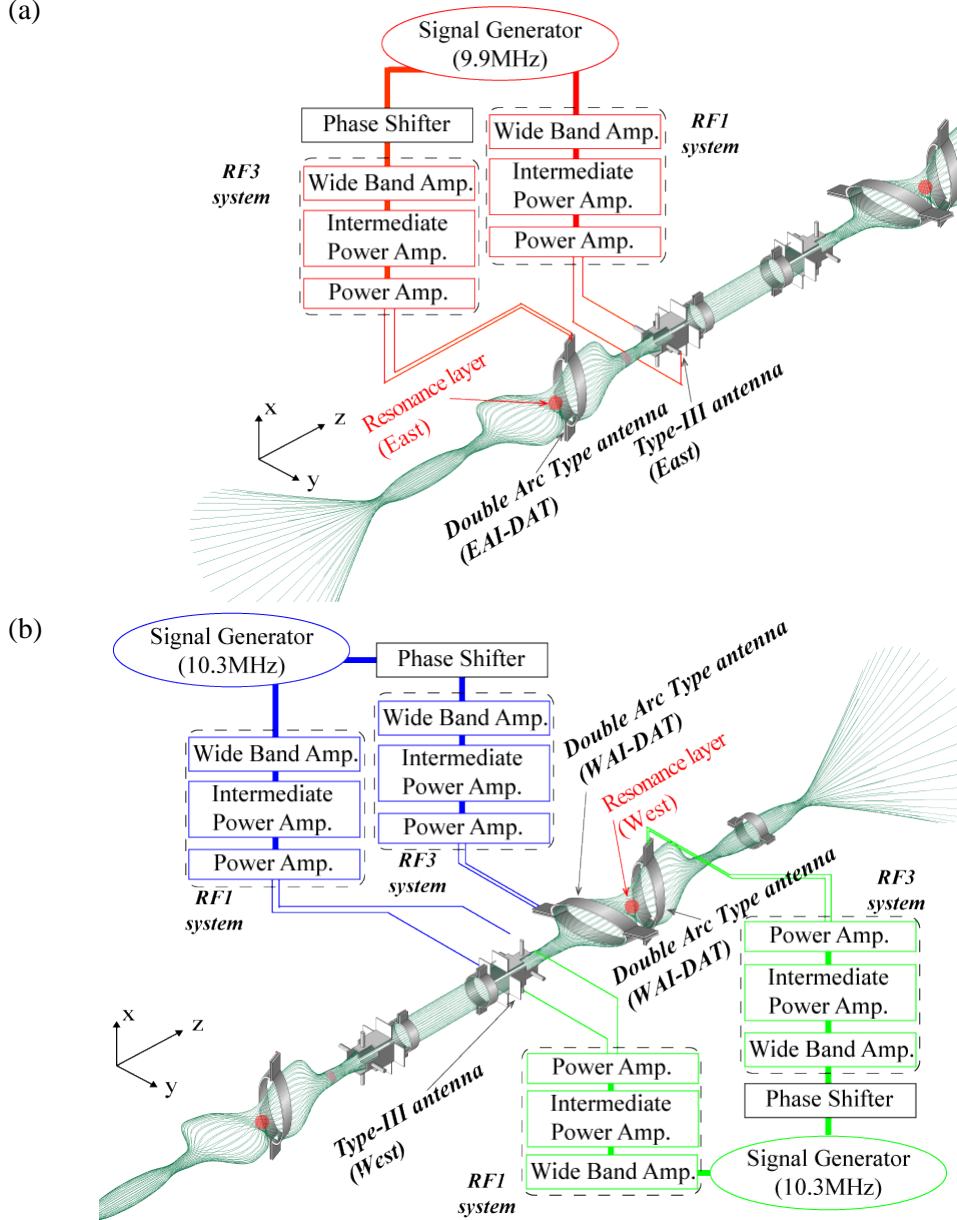


Figure 5.2 Schematic drawing of phase-control experiments in case of (a) Type-III (East) and EAI-DAT antennas with 9.9MHz waves in the east side, and (b) Type-III (West) and WAI-DAT or WAO-DAT antennas with 10.3MHz waves in the west side.

5.3 Anchor Heating in Phase-control Experiments

In order to control and enhance ion-heating in the anchor cell, the phase-control experiments are performed in three conditions. In these experiments, effects of wave propagation in the anchor cell is measured by SED signal installed in the anchor cell, because we are considering that SED signal shows the heating effect of ICRF waves. ICRF waves near 10.0MHz are used for ion-heating and plasma production. The signal of SED includes the information of charge exchange neutrals and emissions from the plasmas.

In this experiments, Type-III antenna at the east side of the central cell ($z=-2.2\text{m}$) and EAI-DAT

antenna ($z=-4.93\text{m}$) are used with 9.9MHz ICRF waves. The distance between both antennas is about 2.73m. Figure 5.3 shows the temporal evolution of (a) Diamagnetism in the central cell, (b) Line-integrated density in the central cell, (c) SED signal in the east anchor cell, and (d) Phase-difference of antenna current between Type-III (East) and EAI-DAT antennas. The blue mask indicates the injection period of RF power from EAI-DAT antenna.

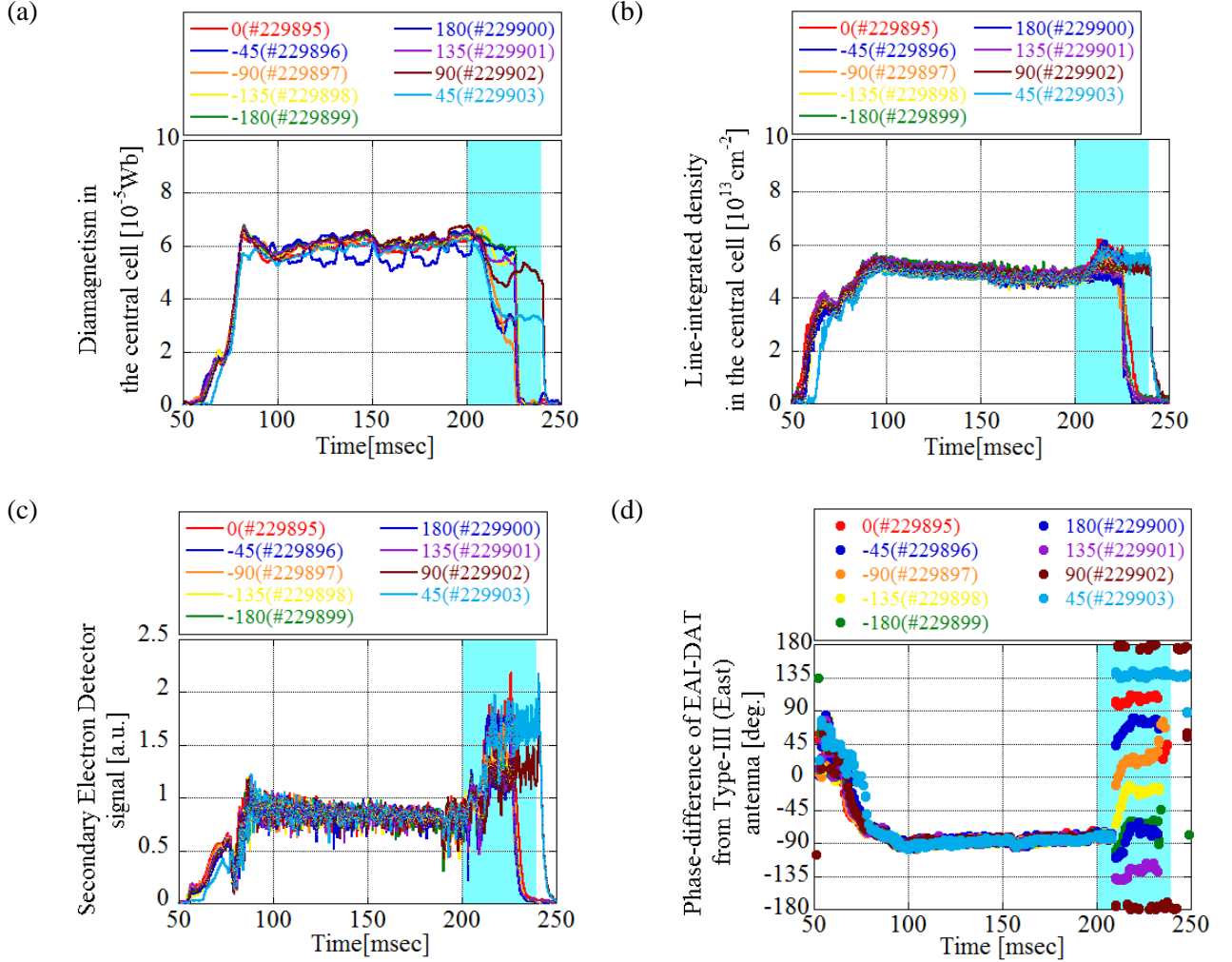


Figure 5.3 Temporal evolution of (a)Diamagnetism in the central cell, (b)Line-integrated density in the central cell, (c) SED signal in the east anchor cell, and Phase-difference of antenna current between Type-III (East) and EAI-DAT antennas. The blue mask indicates the injection time of RF power from WAI-DAT antenna.

In this experiments, Type-III antenna at the west side of the central cell ($z=2.2\text{m}$) and WAI-DAT antenna ($z=4.93\text{m}$) are used with 10.3MHz ICRF waves. The distance between both antennas is about 2.73m. Figure 5.4 shows the temporal evolution of (a) Diamagnetism in the central cell, (b) Line-integrated density in the central cell, (c) SED signal in the west anchor cell, and (d) Phase-difference of antenna current between Type-III (East) and WAI-DAT antennas. The blue mask indicates the injection period of RF power from WAI-DAT antenna.

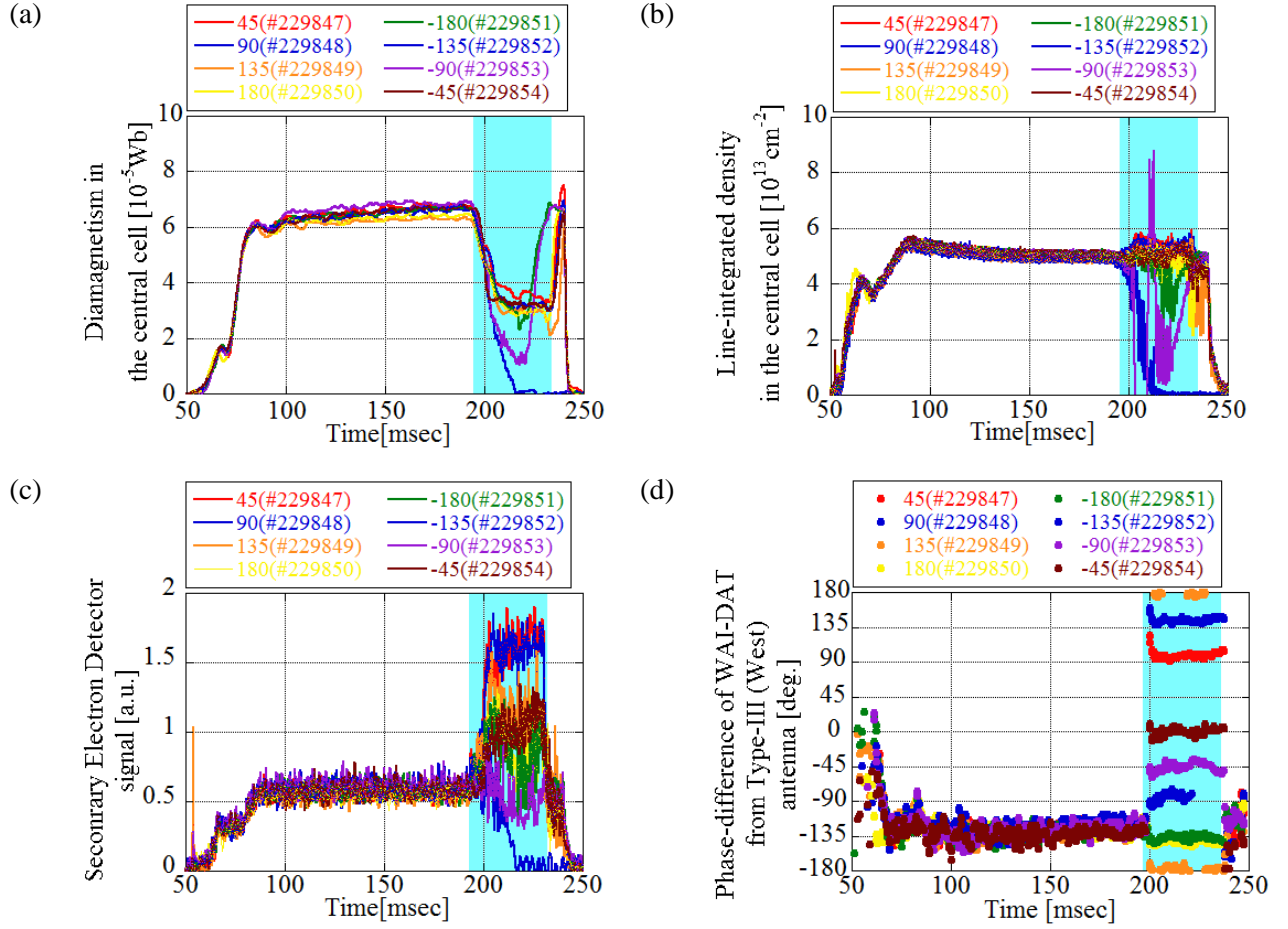


Figure 5.4 Temporal evolution of (a) Diamagnetism in the central cell, (b) Line-integrated density in the central cell, (c) SED signal in the west anchor cell, and (d) Phase-difference of antenna current between Type-III (West) and WAI-DAT antennas. The blue mask indicates the injection time of RF power from WAI-DAT antenna.

In this experiments, Type-III antenna at the west side of the central cell ($z=2.2$ m) and WAO-DAT antenna ($z=5.47$ m) are used with 10.3MHz ICRF waves. The distance between both antennas is about 3.27m. Figure 5.5 shows the temporal evolution of (a) Diamagnetism in the central cell, (b) Line-integrated density in the central cell, (c) SED signal in the west anchor cell, and (d) Phase-difference of antenna current between Type-III (West) and WAO-DAT antennas. The blue mask indicates the injection period of RF power from WAO-DAT antenna.

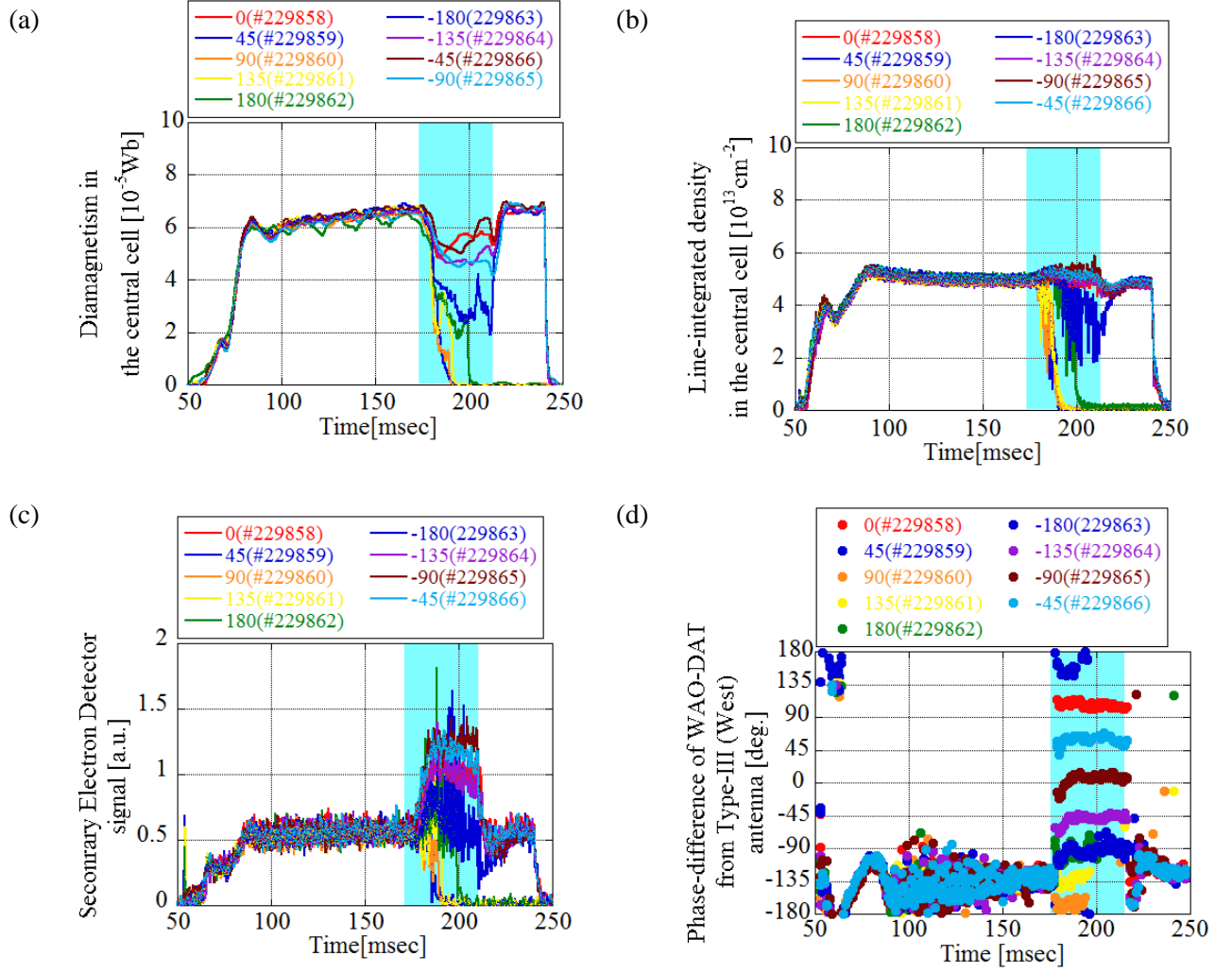


Figure 5.5 Temporal evolution of (a)Diamagnetism in the central cell, (b)Line-integrated density in the central cell, (c) SED signal in the west anchor cell, and (d) Phase-difference of antenna current between Type-III (West) and WAO-DAT antennas. The blue mask indicates the injection time of RF power from WAI-DAT antenna.

The increase of line-integrated density in the central cell and SED signal in the east anchor cell are observed in the each cases of the phase control experiments. The phase difference of antenna current is measured by the single pick-up coil installed near the Type-III antennas and the anchor antennas as shown in Fig. 5.3(d), Fig. 5.4(d), and Fig. 5.5(d). It is observed in the experiments that plasmas can't keep by changing phase difference of antenna current. It is considered that the decrease of anchor heating by wave inference in phase control experiments is the one of the reason. The drop of the diamagnetism in the central cell appears in the phase control experiments. It is considered as a one of the reason that the ion heating at the central cell by DHT antennas with 6.36MHz waves decreases by shifting of the resonance layer by the diamagnetic effect by the increase of the density in the central cell [35].

5.4 Wave Propagation in Phase-control Experiments

Figure 5.6 shows the phase difference dependence of (a) the normalized line integrated density and the diamagnetism in the central cell and (b) the normalized line integrated density and SED signal in the anchor cell in cases of Type-III (East) and EAI-DAT antennas. Figure 5.6 (c) and (d) show those in case of Type-III (West) and WAI-DAT antennas. Figure 5.6(e) and (f) show those in case of Type-III (West) and WAO-DAT antennas. The parameters in the central cell such as the diamagnetism and the line-integrated density are shown in left side, on the other hand, these in anchor cell such as the SED signal and the line-integrated density are shown in the right side, respectively. From Fig. 5.6(b) and (d), it is observed that the increase of SED signal is performed near $\delta=90$ in cases of Type-III (East) and EAI-DAT antennas and Type-III (West) and WAI-DAT antennas. From Fig. 5.6(f), that is performed near $\delta=0$ in the case of Type-III (West) and WAO-DAT antennas. The difference of the phase difference of the increase of SED signal in case of Fig. 5.6(d) and (f) is $\delta=90$. It is considered that this difference is caused by the configuration between two antennas and the resonance layer and the difference of antenna current of WAI-DAT antenna and WAO-DAT antenna. From this results, it becomes clear that the enhancement of ion-heating and producing plasmas in the anchor cell is performed when ICRF waves propagate to the anchor cell. The increase of line-integrated density in the anchor cell as shown in Fig. 5.6(b) is larger than that in Fig. 5.6(d). In case of Fig. 5.6(b), 9.9MHz waves are used for phase control experiments. It is considered as a one of the reason that the resonance layer of 9.9MHz waves exists near the midpoint of the anchor cell than that of 10.3MHz waves, so the density at the resonance layer of 9.9MHz wave is larger than that of 10.3MHz waves. And it is also clearly observed that the phase difference dependence of the line-integrated density in the anchor cell is same as the SED signal. The phase difference dependence of the line-integrated density in the central cell is also same as that in the anchor cell. This effect may be caused by enhancement of confinement plasmas by enhancement of ion-heating in the anchor cell. The increase of SED signal in the case of Type-III and WAI-DAT antennas is larger than that in the case of Type-III and WAO-DAT antennas.

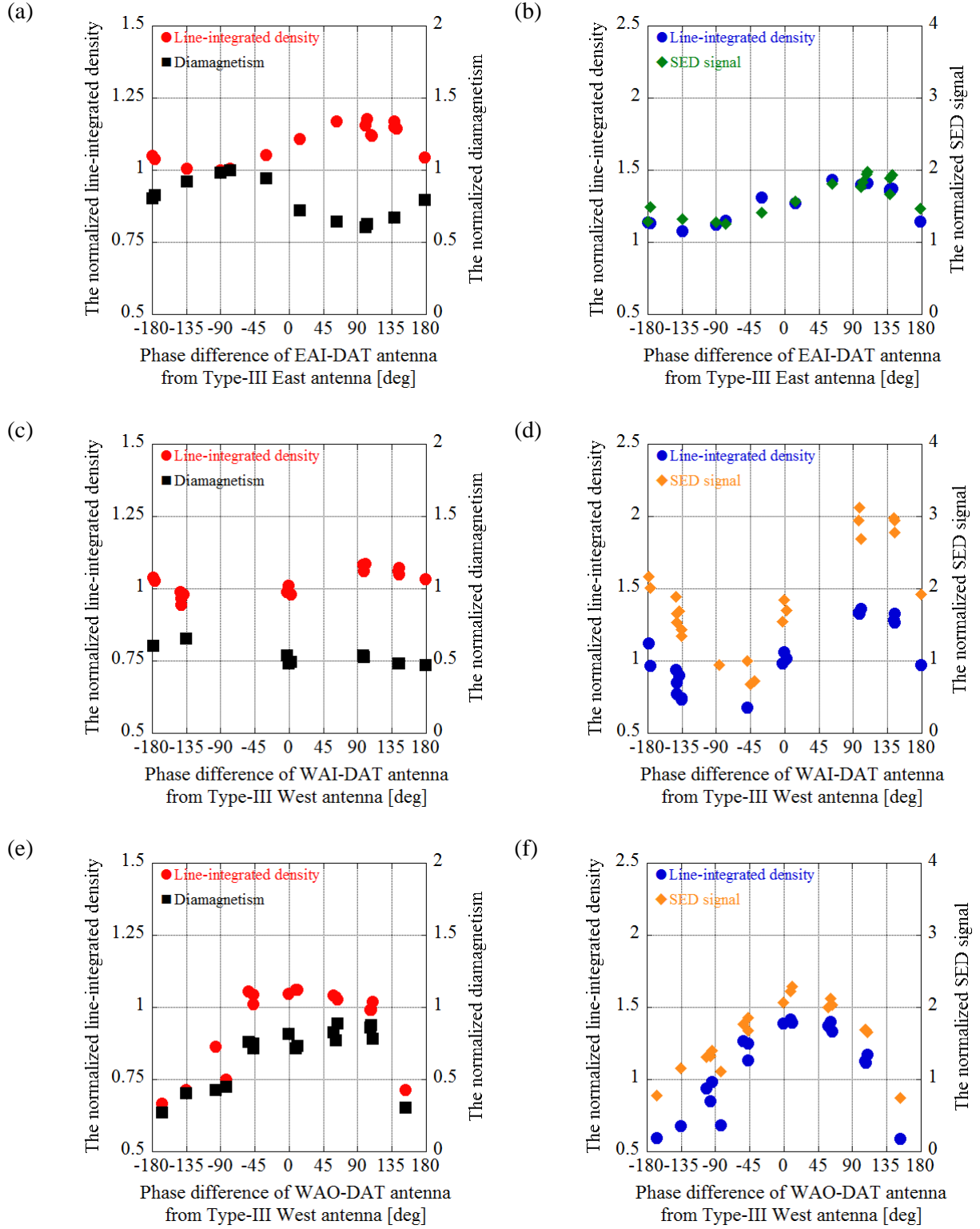


Figure 5.6 Phase difference dependence of the normalized line integrated density and the diamagnetism in the central cell in case of (a) Type-III (East) and EAI-DAT antennas, (c) Type-III (West) and WAI-DAT antennas, and (e) Type-III (West) and WAO-DAT antennas, and the normalized line integrated density and SED signal in the anchor cell in case of (b) Type-III (East) and EAI-DAT antennas, (d) Type-III (West) and WAI-DAT antennas, and (f) Type-III (West) and WAO-DAT antennas.

5.5 Producing High Density Plasmas with Phase-control

In phase control experiments, the increase line-density with the additional gas puffing is performed. In this experiments, the additional gas is injected to plasmas from GP#1a at the east side or GP#2a at the west side during RF waves from the anchor ICRF antenna. Figure 5.7 shows (a) typical time evolution of the line-integrated density in the east anchor cell, and (b) the pressure of additional gas dependence of the line-integrated density in the east anchor cell in the phase control experiments with Type-III antenna in the east side and EAI-DAT antenna. In the Fig. 5.7(a), the yellow mesh indicates the period during RF power by EAI-DAT antenna. The increase line-integrated density in the east anchor cell is observed with the increase of the additional gas.

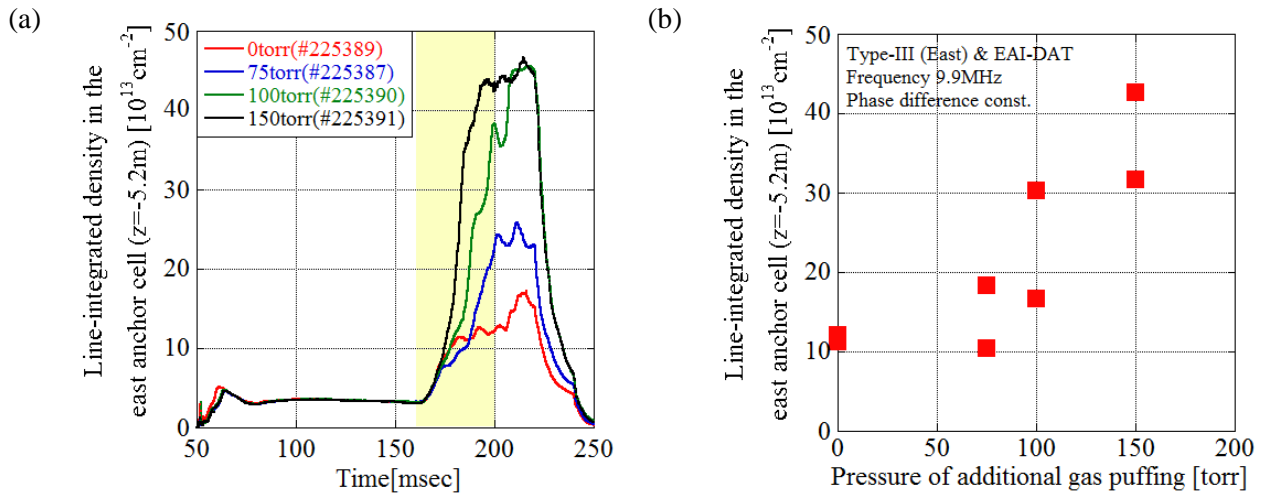


Figure 5.7 (a) Typical time evolution of the line-integrated density in the east anchor cell, and (b) the pressure of additional gas dependence of the line-integrated density in the east anchor cell in the east side phase control experiments

Chapter 6

Wave Analysis by TASK/WF

In order to analyze the wave propagation in the phase-control experiments, TASK/WF code is used for the calculation of the absorbed powers as a function of the phase difference between two antennas

6.1 Typical Excited Waves for Anchor Heating

In the numerical simulation, electron density is determined $2.0 \times 10^{18} \text{m}^{-3}$ at the midpoint of the central cell and the west anchor cell, and $1.2 \times 10^{18} \text{m}^{-3}$ at the midpoint of the mirror throat of the central cell as shown in Chapter 3. Figure 6.1 shows the contour map of the absorbed power of ions in the simulation of the phase control experiments in the case of Type-III and WAI-DAT antennas with 10.3MHz waves. The phase difference of Type-III and WAI-DAT antenna is selected as the enhancement of ion-heating in the anchor cell. In Fig. 6.1, the red lines are indicated the plasma region. The absorbed power is calculated as shown in Eq. (3.26) in TASK/WF. It is clearly observed that the closed resonance layer exists in the anchor cell.

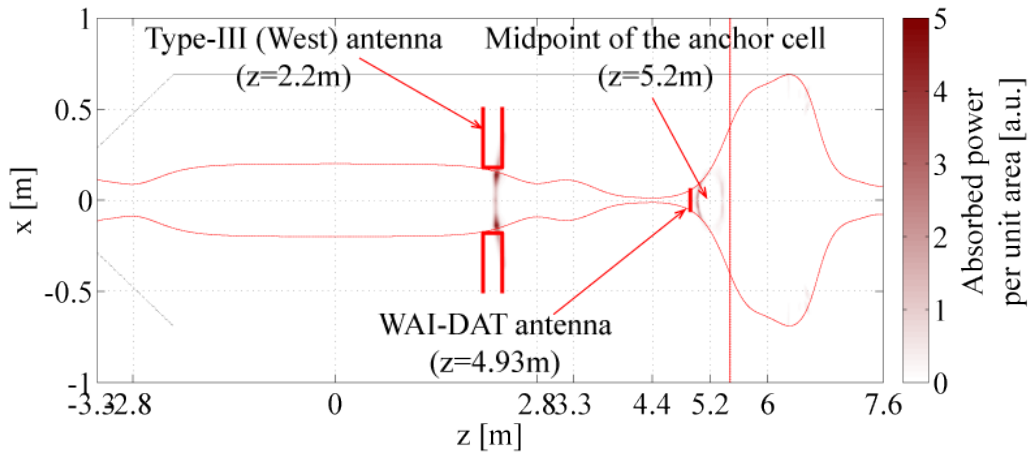


Figure 6.1 The contour map of the absorbed power of ions in the simulation of the phase control experiments in the case of Type-III and WAI-DAT antennas. It is clearly observed that the closed resonance layer exists in the anchor cell.

6.2 Simulation of Phase Control Experiments by GAMMA 10 Configuration

6.2.1 Effect of relative location of ICRF antennas and the resonance layer

Figure 6.2 shows the phase difference dependence of the absorbed power at the plasma region ($R_{cc}=0\sim 0.18m$) of the central cell ($-2.8<z<2.8m$), and the anchor cell ($4.4<z<6.0m$) in case of (a) Type-III (West) antenna and WAI-DAT antennas, and (b) Type-III (West) antenna and WAO-DAT antennas using 10.3MHz ICRF waves and $2.0\times 10^{18}m^{-3}$ core density. In this calculation, ICRF waves are excited with 10.3MHz from Type-III antenna and WAI-DAT or WAO-DAT antenna with phase controlling. In the Fig.6.2 the phase difference is determined based on the Type-III antenna. The resonance layer of 10.3MHz waves in the west anchor cell exists at the right side of both antennas in the case of Type-III (West) antenna and WAI-DAT antennas, in contrast, between both antennas in the case of Type-III (West) antenna and WAO-DAT antennas. Here, in TASK/WF, plasmas are assumed as for the steady state, and the cold model including collision effects, so the absolute value of the absorbed power cannot be found and the effects by plasma temperature cannot be calculated exactly. However, in the previous research, the slow wave is absorbed approximately completely at the resonance layer with the gently sloping magnetic gradient [50, 51, 52]. From the absorbed power in the central cell and the anchor cell, the amount of change in case of Type-III and WAI-DAT antenna as shown in Fig. 6.2(a) is larger than that in case of Type-III and WAO-DAT antenna as shown in Fig. 6.2(b). In this calculation, it is selected as the absorbed power by the cyclotron damping is larger than that by the collision damping. In this condition, it is considered as a one of the reason for the small change of the absorbed power in Fig. 6.2(b) that the decrease of ICRF waves for wave inference by existing the resonance layer of 10.3MHz between two antenna.

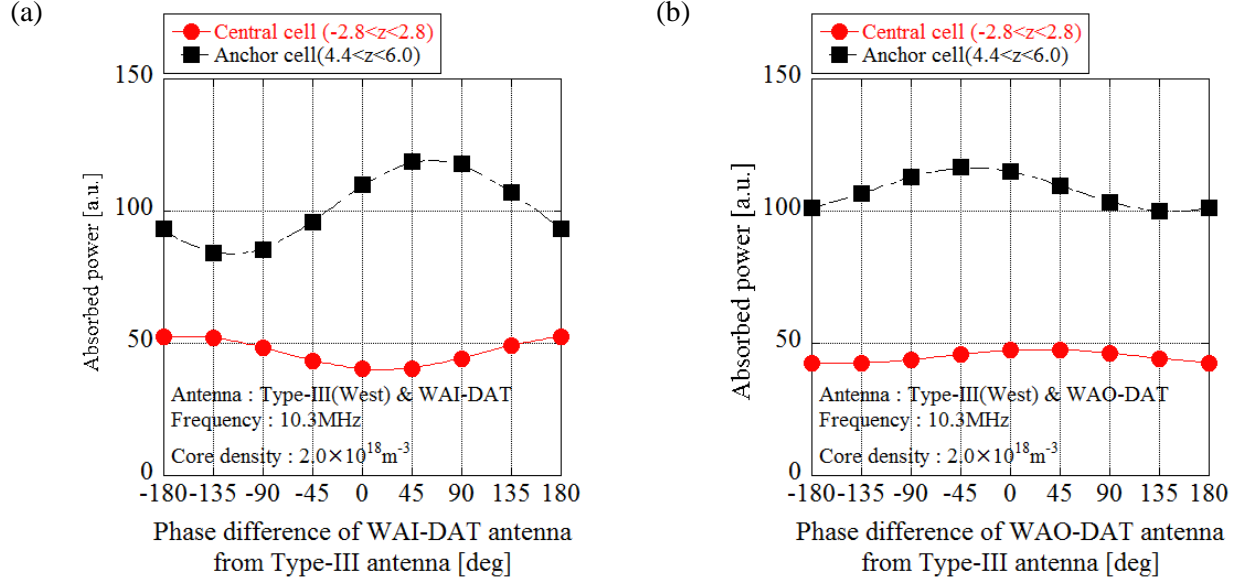


Figure 6.2 Phase difference dependence of the absorbed power at the plasma region ($R_{cc}=0\sim0.18\text{m}$) of the central cell ($-2.8 < z < 2.8\text{m}$), and the anchor cell ($4.4 < z < 6.0\text{m}$) in case of (a) Type-III (West) antenna and WAI-DAT antennas, and (b) Type-III (West) antenna and WAO-DAT antennas using 10.3MHz ICRF waves and $2.0 \times 10^{18} \text{ m}^{-3}$ core density.

We consider the phase difference dependence of the absorbed power in the phase control experiment. From Fig 6.2, in this condition, it is observed that the increase of the absorbed power at the anchor cell is performed at $\delta=45\sim90$ in case of Type-III and WAI-DAT antennas, and at $\delta=-45\sim0$ in case of Type-III and WAO-DAT antennas, and the increase of the absorbed power in the central cell is performed in the different phase difference in both cases of WAI-DAT and WAO-DAT antennas.

By using the results of the experiments as shown in Fig. 5.6 and the those of the numerical simulation as shown in Fig. 6.2, the effects of ion heating in the anchor cell are discussed. The phase difference of Type-III antenna and WAI-DAT or WAO-DAT antenna is measured in the experiments and selected in the numerical simulation as same value. The change of the absorbed power is measured as the change of SED signal in the experiments. The SED signal in Fig. 5.6(d) and the absorbed power at the anchor cell in Fig. 6.2(a), which are shown in the case of Type-III and WAI-DAT antennas, become large at the same phase difference near $\delta=90$. On the other hand, The SED signal in Fig. 5.6(f) and the absorbed power at the anchor cell in Fig. 6.2(b), which are shown in the case of Type-III and WAO-DAT antennas, becomes large at the same phase difference near $\delta=0$. It becomes clear that the enhancement of ion-heating in the anchor cell is performed with wave propagation in the anchor cell. On the other hand, the increase of line-integrated density in the central cell and that in the anchor cell is performed at same phase-difference in the experiments. However, the increase of the absorbed power in the central cell is performed at $\delta=-180$ in the case of Type-III (West) and WAI-DAT antennas. From these results, it is considering that the increase of the line-integrated density in the central cell is performed by the enhancement of the ion-heating in the anchor cell.

6.2.2 Density dependence of Phase Control Experiments

It is important to evaluate density dependence of increase ion-heating, because wave number has density dependence. In order to investigate about the density dependence, the phase difference dependence of the absorbed power at the central cell and the anchor cell is calculated in case of Type-III and WAI-DAT antenna. In case of Type-III and WAI-DAT, the resonance layer don't exist between two antennas, so the effects of wave influence is not affected by the resonance layer in the anchor cell. Figure 6.3 shows the phase difference and density dependence of the absorbed power (a) at the central cell ($-2.8 < z < 2.8\text{m}$) and (b) the anchor cell ($4.4 < z < 6.0\text{m}$), in case of Type-III (West) antenna and WAI-DAT antennas. The profile of electron density and the magnetic field strength is fixed in this calculation. From Fig. 6.3(a) and (b), it is observed that the phase-difference of increase the absorbing power is shifted to large value of phase-difference at left side of both antennas, on the other hand, that is shifted to small value at right side of both antennas. The direction of shifting of the phase difference with the increase of the electron density is same direction in simple model as shown in Eqs. (5.1), (5.2), and (5.3). According to the simple model, the phase difference of the increase of the absorbed power at the left side of both antennas, where the central cell is same location in the experiments, is shifted to large value of phase-difference with the increase of the wave number, on the other hand, that at the right side of both antennas, where the anchor cell is same location in the experiments, is shifted to small value of the phase-difference. According to these results, it is indicated that the density between antennas is important parameters in phase control experiments, however, it becomes clear that the density dependence of the phase difference of the increase absorbed power is small in these condition.

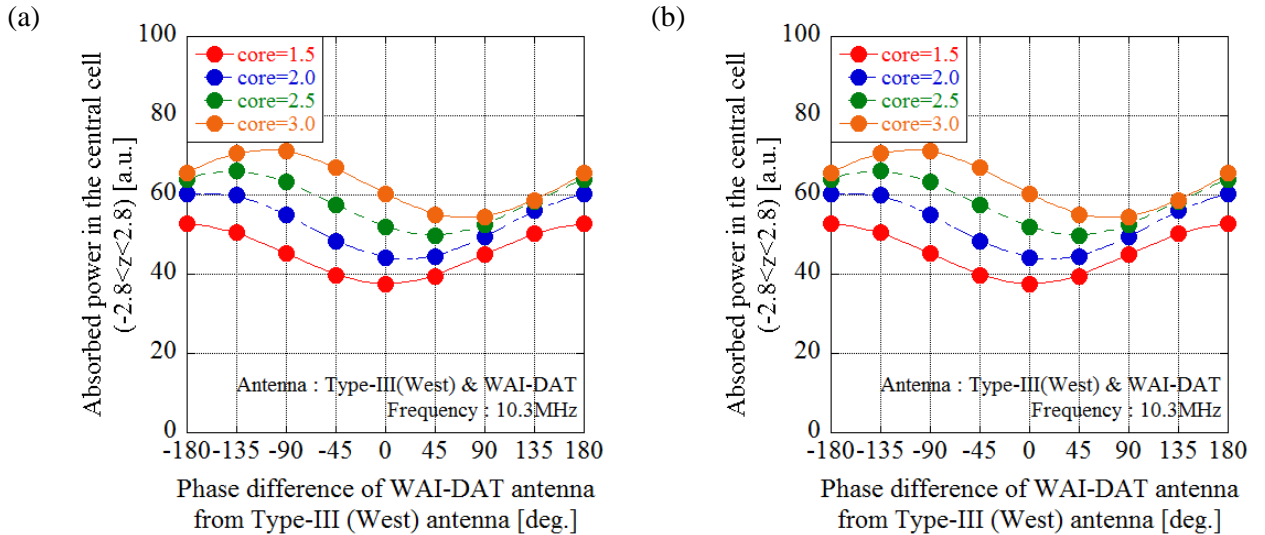


Figure 6.3 Phase difference and density dependence of the absorbed power (a) at the central cell ($-2.8 < z < 2.8\text{m}$) and (b) the anchor cell ($4.4 < z < 6.0\text{m}$), which includes the anchor cell, in case of Type-III (West) antenna and WAI-DAT antennas.

Chapter 7

Conclusion

In the GAMMA 10 tandem mirror, it has been demonstrated that high beta plasma production in the anchor cell with minimum-B configuration is important to keep MHD stability of whole plasmas.

In order to control the ICRF produced plasmas effectively in the anchor cell, the dependence of the antenna configuration and the applied frequency on the antenna loading resistance are calculated with three dimensional full wave code; TASK/WF. It has been evaluated that the shape of the antenna and the applied frequency affect the antenna loading strongly. Double Arc Type (DAT) antennas which are designed to be along the shape of the plasma cross section have been newly installed in the anchor cell. In the numerical simulation, the increase of the antenna loading resistance more than three times is indicated by changing DAT antenna from Bar-type antenna. The increase of the antenna loading more than three times has been confirmed also in the experiments.

Two DAT antennas are installed on both sides of the midplane of the west anchor cell. In the case of the inside antenna near the central cell, the cyclotron resonance layer exists in the right side of both central and anchor antennas. On the other hand, the resonance layer exists between both antennas in the case of the outside antenna near the end region. In order to optimize the ion heating in the anchor cell, the phase control experiments between two antennas installed in the anchor and central cells have been introduced. The enhancement of the ion heating in the anchor cell and the increase of the density in the anchor and central cells are clearly observed depending on the phase difference between two antennas. It is shown in the experiments that the optimum phase difference is almost 90 degrees different value. It is also shown in the experiments that the anchor heating by 9.9MHz waves is performed more effectively than that of 10.3MHz waves.

In order to interpret the experimental results, the absorbed powers on the resonance layer in the phase control experiments are calculated with TASK/WF code. In both anchor antenna cases, the absorbed power depends on the phase difference between two antennas. It is clearly obtained that the phase difference at the maximum absorbed power is that on the optimum condition in the experiments.

According to the results of the anchor heating experiments and the numerical simulation, it is observed that the increase of the antenna loading and the enhancement of anchor heating by phase control between two antennas are achieved. The enhancement of the antenna loading and the optimization of the phase difference between two antennas will be essential for the increase of the plasma performance for the tandem mirror experiments such as the divertor simulation.

Acknowledgment

First of all, the author would like to deeply appreciate Prof. M. Ichimura, Director of Plasma Research Center at University of Tsukuba, who has taught the author ways of thinking and acting as a researcher, and also as one human being during my six years research which was filled with difficulties. What the author has learned through research was all precious experience, and the author is confident that it will be my lifelong heritage. The author appreciates Dr. M. Hirata who has taken good care of her for lecturing experiments, research processes, and also discussions over our research. The author appreciates Dr. R. Ikezoe who is my very close role model and has taught me a lot for five years since the author's master degree course began. The author is really grateful for both of them. The author appreciates staff member Y. Washo who taught me the settings and maintenance of the server and calculator for six years. The author thanks to my research group seniors, S. Sato, Y. Imai, T. Murakami who have taught me a lot through group activities such as discussion, GAMMA 10 experiments, and so on. The author thanks to T. Iwai who was always by my side joining the international conference, writing our first scholarly treatise. The author thanks Y. Ugajin, T. Sato, T. Imura, Y. Saito, A. Shiratani, Y. Annaka, Y. Iwamoto, S. Sumida, T. Okada, K. Watanabe, K. Takeyama, S. Jang who have all spent research time with the author, and supported very well in experiments, discussion meeting, and so on. The author would also like to thank Dr. Y. Yamaguchi, assistant professor at Research Center for Development of Far-Infrared Region in University of Fukui. Since the author joined the research group, he taught me the numerical simulation; TASK/WF, the experiments, and at the same time he has shown how to act as a professional researcher.

The author appreciates Profs. T. Imai, Y. Nakashima, I. Katanuma who have gave me lecture very kindly, and also looked after this thesis. Additionally, the author would like to appreciate all professors especially Prof. M. Sakamoto, members of Plasma Research Center. They have shown great support on discussions in Group Meeting, GAMMA10 experiments, the numerical simulations and so on, and provided a sophisticated environment for this research.

The author deeply appreciates Prof. A. Fukuyama at the Department of Nuclear Engineering in Kyoto University provided TASK code and cared even though the author is a foreign student on the bidirectional collaborative research program of National Institute for Fusion Science (NIFS). The author is blessed to have a chance to research with world's authoritative researchers and see the forefront of nuclear fusion research. Prof. A. Ando at Tohoku University and Prof. S. Shinohara at Tokyo University of Agriculture and Technology gave the author directions during GAMMA10 experiments on the bidirectional collaborative research program of NIFS. The author appreciates them.

The author has spent six and five years with students of the same school year, H. Takeda, K. Ichimura. The time we've spent together chatting, discussing about "Nuclear Fusion", and encouraging each other to

achieve the doctoral degree was very precious. The author appreciates them very well. During six years at Plasma Research Center, the author has discussed and experimented with over one hundred students about "Nuclear Fusion". When the author served as a student leader for two years from 2012, it was a very precious opportunities to learn how hard it is to cooperate and manage a large size of research, and considering one thing in many ways at the same time. The author was blessed to have a chance researching and studying about future energy "Nuclear Fusion" at Plasma Research Center. It is precious experiences.

During ten year life at Tsukuba, the author has met a lot of people beginning from clubs and part time job the author belonged to, and also at favorite place "WAKATARO", and "cin-cin". Throughout daily life chatting about "Nuclear Fusion" and "Energy" gave me new inspirations. The research was very heavy loaded, but chatting with friends who has different mind thinking enriched living and left good memories. All the time the author spent discussing about energy and research will also be treasure throughout life. When the author first came to "Tsukuba" ten years ago, the Tsukuba Express line wasn't running yet. The author has never imagined how capable the author could be. Gaining and also losing irreplaceable things, was a priceless life experience. The author thanks all who have supported me during ten year life. Especially, the younger students in the master's course and the colleagues are the reassuring support. The author hopes this thesis could be a some guidepost for whomever it concerns, especially to those who has a will to challenge the doctoral degree.

Finally, the author thanks his family and all beloved ones for watching over selfish acts so warmly for 23 years of education term

This work is partially supported by the bidirectional collaborative research program of National Institute for Fusion Science, Japan.

Bibliography

- [1] Dale Meade, "50 years of fusion research," Nuclear Fusion, **50**, p. 014004, 2010.
- [2] K. Yoshizuka, and M. Kondo, "Recovery of Lithium from Seawater," Journal of Plasma and Fusion Research, **87**, 12, pp. 795-800, 2011.
- [3] K. Ooi, "Technology on the Lithium Recovery from Seawater (1) Adsorbent for Lithium," Bulletin of the Society of Sea Water Science, Japan, **51**, 5, pp. 285-288.
- [4] H. Nobukawa, "Technology on the Lithium Recovery from Seawater (2) Extraction System and Simulation," Bulletin of the Society of Sea Water Science, Japan, **51**, 5, pp. 289-292, 1997.
- [5] K. Tokimatsu, Y. Asaoka, S. Konishi, J. Fujino, Y. Ogawa, K. Okano, S. Nishio, T. Yoshida, R. Hiwatari and K. Yamaji, "Studies of breakeven prices and electricity supply potentials of nuclear fusion by a long-term world energy and environment model," Nuclear Fusion, **42**, pp. 1289-1298, 2002.
- [6] Koji Tokimatsu, Jun'ichi Fujino, Satoshi Konishi, Yuichi Ogawa, and Kenji Yamaji, "Role of nuclear fusion in future energy systems and the environment under future uncertainties," Energy Policy, **31**, pp. 775-797, 2003.
- [7] J. Wesson, Tokamaks Fourth edition, OXFORD UNIVERSITY PRESS, 2011.
- [8] R. Hiwatari, K. Okano, Y. Asaoka, K. Shinya and Y. Ogawa, "Demonstration tokamak fusion power plant for early realization of net electric power generation," Nuclear Fusion, vol. 45, pp. 96-109, 2005.
- [9] Bo Lehnert, "Half a century of fusion research towards ITER," Physica Scripta, **87**, 018201, 2013.
- [10] H. Takatsu, "ITER project and fusion technology," Nuclear Fusion, **51**, p. 094002, 2011.
- [11] Y. Shimomura, R. Aymar, V. Chuyanov, M. Huguet, R. Parker, ITER Joint Central Team, "ITER overview," Nuclear Fusion, **39**, 9Y, pp. 1295-1308, 1999.
- [12] T. Tamano, "Tandem mirror experiments in GAMMA 10," Physics of Plasmas, **2**, 6, pp. 2321-2327, 1995.
- [13] K. Yatsu, L.G. Bruskin, T. Cho, M. Hamada, M. Hirata, H. Hojo, M. Ichimura, K. Ishi, A. Itakura, I. Katanuma, Y. Kiwamoto, J. Kohagura, S. Kubota, A. Mase, Y. Nakashima, T. Sato, Y. Sakamoto, T. Tamano, Y. Tatematsu, T. Tokuzawa, and M. Yoshikawa, "Plasma confinement in the GAMMA 10 tandem mirror," Nuclear Fusion, **39**, 11Y, pp. 1707-1712, 1999.
- [14] T. Imai, and GAMMA 10 group, "New Program and Boundary Plasma Research in GAMMA 10 Modification (GAMMA-PDX)," J. Plasma Fusion Res., **87**, 11, pp. 752-786, 2011.
- [15] T. Imai, M. Ichimura, Y. Nakashima, M. Sakamoto, I. Katanuma, M. Yoshikawa, T. Kariya, M. Hirata, J. Kohagura, R. Minami, T. Numakura, R. Ikezoe, K. Oki, K. Sakamoto, and GAMMA 10 group,

- “GAMMA 10/PDX PROJECT STATUS AND FUTURE,” Transactions of Fusion Science and Technology, **63**, 1T, pp. 8-15, 2013.
- [16] Y. Nakashima, M. Ichimura, I. Katanuma, M. Yoshikawa, T. Kariya, R. Minami, Y. Kiwamoto, Y. Miyata, H. Shidara, Y. Yamaguchi, R. Yonenaga, H. Takeda, T. Imai, “Research plan for divertor simulation making use of a large tandem mirror device,” Fusion Engineering and Design, **85**, pp. 956-962, 2010.
- [17] Y. Nakashima, H. Takeda, K. Ichimura, K. Hosoi, M. Sakamoto, M. Hirata, M. Ichimura, R. Ikezoe, T. Imai, T. Ishii, T. Kariya, I. Katanuma, J. Kohagura, R. Minami, T. Numakura, H. Ueda, M. Yoshikawa, N. Asakura, T. Furuta, A. Hatayama, Y. Hirooka, S. Kado,, “Recent results of divertor simulation research using an end-cell of a large tandem mirror device,” Journal of Nuclear Materials, **438**, p. S738–S741, 2013.
- [18] Y. Nakashima, M. Sakamoto, H. Takeda, K. Ichimura, K. Hosoi, K. Oki, M. Yoshikawa, N. Nishino, H. Matsuura, M. Hirata, M. Ichimura, T. Kariya, I. Katanuma, J. Kohagura, R. Minami, T. Numakura, R. Ikezoe, Y. Akabane, S. Kigure, Y. Nagatsuka, S. Takahashi,, “First Results and Future Research Plan of Divertor Simulation Experiments Using D-module in the End-Cell of the GAMMA 10/PDX Tandem Mirror,” Transactions of Fusion Science and Technology, **63**, 1T, pp. 100-105, 2013.
- [19] M. Sakamoto, K. Oki, Y. Nakashima, Y. Akabane, Y. Nagatsuka, M. Yoshikawa, R. Nohara, K. Hosoi, H. Takeda, K. Ichimura, J. Kohagura, M. Yoshikawa, M. Ichimura, and T. Imai, “Plasma Characterization in Divertor Simulation Experiments with a V-Shaped Target on GAMMA 10/PDX,” Transactions of Fusion Science and Technology, **63**, 1T, pp. 188-192, 2013.
- [20] T. Tamano, T. Cho, M. Hirata, H. Hojo, M. Ichimura, M. Inutake, K. Ishii, A. Itakura, I. Katanuma, R. Katsumata, Y. Kiwamoto, A. Mase, Y. Nagayama, Y. Nakashima, T. Saito, M. Shoji, E. Takahashi, Y. Tatematsu, K. Tsuchiya, N. Yamaguchi, K. Yatsu, “Recent Results of Tandem Mirror Experiments in GAMMA 10 and HIEI,” Proc.15th Int. Conf. on Plasma Physics and Controlled Nuclear Fusion Research, Seville, **2**, 399, 1994.
- [21] Y. Nakashima, M. Sakamoto, M. Yoshikawa, H. Takeda, K. Ichimura, K. Hosoi, M. Hirata, M. Ichimura, R. Ikezoe, T. Imai, T. Kariya, I. Katanuma, J. Kohagura, R. Minami, T. Numakura, K. Oki, H. Ueda, N. Asakura, T. Furuta, A. Hatayama, Y. Hirooka, S. Kado, S, “Plasma Characteristics of the End-cell of the GAMMA 10 Tandem Mirror for the Divertor Simulation Experiment,” Proceeding of 24th International Conference on Fusion Energy, San Diego, USA, pp. FTP/P1-11, 2012.
- [22] Y. Nakashima, H. Takeda, K. Ichimura, K. Hosoi, M. Sakamoto, M. Hirata, M. Ichimura, R. Ikezoe, T. Imai, T. Ishii, T. Kariya, I. Katanuma, J. Kohagura, R. Minami, T. Numakura, H. Ueda, M. Yoshikawa, N. Asakura, T. Furuta, A. Hatayama, Y. Hirooka, S. Kado,, “Recent results of divertor simulation research using an end-cell of a large tandem mirror device,” Journal of Nuclear Materials, **438**, pp. S738-S741, 2013.
- [23] M. Ichimura, M. Hirata, R. Ikezoe, T. Yokoyama, Y. Ugajin, T. Sato, T. Iimura, Y. Saito, Y. Annaka, A. Shiratani, M. Yoshikawa, J. Kohagura, Y. Nakashima, K. Ichimura and T. Imai, “RECENT ICRF

- EXPERIMENTS FOR A DIVERTOR SIMULATION STUDY ON GAMMA 10,” Transactions of Fusion Science and Technology, **63**, 1T, pp. 115-118, 2013.
- [24] T. Watari, K. Adati, T. Aoki, S. Hidekuma, K. Hattori, S. Hirose, M. Ichimura, T. Kawamoto, R. Kumazawa, Y. Okubo, S. Okamura, T. Sato, “A slow-wave heating experiment on RFC-XX using an array of phased antennas,” Nuclear Fusion, **22**, 10, pp. 1359-1368, 1982.
- [25] A. Fukuyama, “TASK code Home Page,” [Online]. Available: <http://bpsu.nucleng.kyoto-u.ac.jp/task/>.
- [26] A. Fukuyama, M. Yagi, “Burning Plasma Simulation Initiative and Its Recent Progress,” Journal of Plasma and Fusion Research, **81**, pp. 747-754, 2005.
- [27] T. YAMAMOTO, S. MURAKAMI and A. FUKUYAMA, “Simulation Study of ICRFWave Propagation and Absorption in 3-D Magnetic Configurations,” Plasma and Fusion Research, **3**, S1075, 2008.
- [28] R.V. Budny, L. Berry, R. Bilato, P. Bonoli, M. Brambilla, R.J. Dumont, A. Fukuyama, R. Harvey, E.F. Jaeger, K. Indreshkumar, E. Lerche, D. McCune, C.K. Phillips, V. Vdovin, J. Wright and members of the ITPA-IOS, “Benchmarking ICRF full-wave solvers for ITER,” Nuclear Fusion, **52**, 2012.
- [29] A. FUKUYAMA, N. OKAZAKI, A. GOTO, S.-I. ITOH, and K. ITOH, “Propagation and absorption of ICRF waves in helical plasmas,” Nuclear Fusion, **26**, 2, pp. 151-162, 1986.
- [30] R.J. Dumont and D. Zarzoso, “Heating and current drive by ion cyclotron waves in the activated phase of ITER,” Nuclear Fusion, **53**, 013002, 2013.
- [31] A. Fukuyama, and M. Yagi, “Burning Plasma Simulation Initiative and Its Recent Progress,” Journal of Plasma and Fusion Research, **81**, 10, pp. 747-754, 2005.
- [32] A. Fukuyama, “Role of Simulation in Remote Experiments,” Journal of Plasma and Fusion Research, **89**, 7, pp. 479-481, 2013.
- [33] T. Imai, “Recent Progress of the ECH Experiments in Mirror Devices,” J. Plasma Fusion Research, **85**, 6, pp. 378-382, 2009.
- [34] K. Hosoi, Master's thesis, University of Tsukuba, 2011.
- [35] T. YOKOYAMA, M. ICHIMURA, R. IKEZOE, Y. UGAJIN, T. IWAI, T. SATO, T. IIMURA, Y. SAITO, M. HIRATA, Y. YAMAGUCHI, A. FUKUYAMA and T. IMAI, “Improvement of ICRF Antenna Loading in the Minimum-B Configuration on GAMMA 10,” Plasma and Fusion Research, **7**, 2402136, 2012.
- [36] T. Yokoyama, M. Ichimura, Y. Ugajin, Y. Saito, A. Fukuyama, Y. Yamaguchi, M. Hirata, R. Ikezoe, T. Sato, T. Iimura, Y. Annaka, A. Shiratani and T. Imai, “ICRF ANTENNA LOADING IN THE MINIMUM-B ANCHOR CONFIGURATION ON GAMMA 10,” Transactions of Fusion Science and Technology, **63**, 1T, pp. 268-270, 2013.
- [37] S. Miyoshi, Mirror-gata Kakuyuugo Sochi (Magnetic mirror fusion experiment), IPC, 1995.
- [38] H. Hojo, M. Inutake, M. Ichimura, Y. Kimura, and S. Miyoshi, “Coupled Alfvén Waves in a Quadrupole Magnetic Field and Mode Conversion,” Physical Review Letters, **66**, 14, pp. 1866-1869, 1991.
- [39] M. Inutake, M. Ichimura, H. Hojo, Y. Kimura, R. Katsumata, S. Adachi, Y. Nakashima, A. Itakura, A.

- Mase, and S. Miyoshi, "Polarization Reversal of Alfvén Waves in a Nonaxisymmetric Region of a Quadrupole-Anchored Tandem Mirror," *Physical Review Letters*, **65**, 27, pp. 3397-3400, 1990.
- [40] M. ICHIMURA, M. INUTAKE, S. ADACHI, D. SATO, F. TSUBOI, Y. NAKASHIMA, I. KATANUMA, A. ITAKURA, A. MASE, and S. MIYOSHI, "Anchor plasma buildup by using central cell ICRF antennas in the tandem mirror GAMMA 10," *Nuclear Fusion*, **28**, 5, pp. 799-807, 1988.
- [41] H. Hojo, "Flute-Mode Stability of Quadrupole-Anchored Tandem Mirror Plasmas," *Plasma and Fusion Research*, **5**, 008, 2010.
- [42] M. Ichimura, M. Inutake, R. Katsumata, A. Ishihara, A. Mase, H. Hojo, K. Ishii, Y. Nakashima, I. Katanuma, T. Tamano, "Stability of ICRF-heated plasmas in the GAMMA 10 tandem mirror," *Fusion Engineering and Design*, **26**, pp. 251-258, 1995.
- [43] R. Katsumata, M. Inutake, M. Ichimura, N. Hino, H. Onda, I. Katanuma, H. Hojo, A. Mase, and S. Miyoshi, "Temperature Anisotropy Measurement Using Diamagnetic Loop Array," *Journal of Applied Physics*, **31**, 7, pp. 2249-2254, 1992.
- [44] S. Tanaka, M. Ichimura, S. Takayama, M. Inutake, S. Kanazawa, M. Nakamura, E. Ishikawa, C. Satake, S. Motegi, T. Saito, H. Hojo, A. Mase, K. Ishii, T. Tamano, and K. Yatsu, "Low frequency fluctuations measured by probes in the GAMMA10 tandem mirror," *Review of Scientific Instruments*, **70**, 1, pp. 979-982, 1999.
- [45] A. Fukuyama, S. Murakami, M. Honda, Y. Izumi, "Advanced Transport Modeling of Toroidal Plasmas with Transport Barriers," *Proceeding of 20th IAEA Fusion Energy Conference 2004* (IAEA, Vienna, 2005).
- [46] Thomas H. Stix, "Waves in Plasmas: Highlights from the Past and Present," 1984.
- [47] Y. Yamaguchi, M. Ichimura, T. Yokoyama, A. Fukuyama, R. Ikezoe, Y. Imai, T. Murakami, T. Iwai, T. Sato, Y. Ugajin and T. Imai, "ION-CYCLOTRON RESONANCE HEATING EXPERIMENT IN THE QUADRUPLE MINIMUM-B FIELD ON GAMMA 10," *Transaction of Fusion Science and Technology*, **59**, 1T, p. 250, 2011.
- [48] Y. UGAJIN, M. Ichimura, T. Yokoyama, Y. Saito, M. Hirata, R. Ikezoe, T. Sato, T. Iimura, Y. Annaka, A. Shiratani, Y. Nakashima, R. Minami, and T. Imai, "ICRF Experiment with Phase-controlled Antennas on GAMMA10," *Transactions of Fusion Science and Technology*, **63**, 1T, pp. 268-270, 2013.
- [49] Y. Saito, M. Ichimura, T. Yokoyama, Y. Ugajin, , M. Hirata, R. Ikezoe, T. Sato, T. Iimura, A. Shiratani, Y. Annaka, Y. Nakashima, and T. Imai, "ICRF HEATING EXPERIMENTS IN BOTH EAST AND WEST ANCHOR CELLS ON GAMMA10," *Transactions of Fusion Science and Technology*, **63**, 1T, pp. 277-279, 2013.
- [50] A. Fukuyama, K. Itoh, and S.-I. Itoh, "GLOBAL WAVES IN HOT PLASMAS," *Computer Physics Report*, **4**, pp. 137-181, 1986.
- [51] A. Fukuyama, T. Matsuishi and Y. Furutani, "Kinetic Analysis of Wave Propagation and Absorption near Cyclotron Resonance," *Journal of Physical Society of Japan*.

- [52] A. Fukuyama, "Quantitative Analysis of Wave Absorption near Cyclotron Resonance in an Inhomogeneous Magnetic Field," Results of research report of Grant-in-Aid for Scientific Research, 1986.